

# Relating hydro-mechanical and elastodynamic properties of dynamically-stressed tensile-fractured rock in relation to fracture aperture and contact area

Clay Wood<sup>1</sup>, Prabhakaran Manogharan<sup>2</sup>, Andy Rathbun<sup>3</sup>, Jacques Rivière<sup>2</sup>, Derek Elsworth<sup>2</sup>, Chris Marone<sup>2</sup>, and Parisa Shokouhi<sup>2</sup>

<sup>1</sup>Penn State University

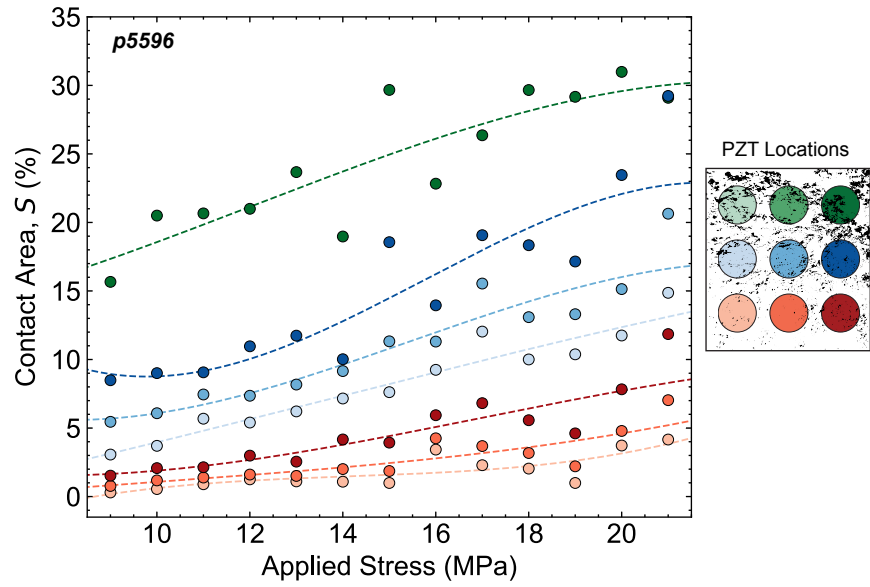
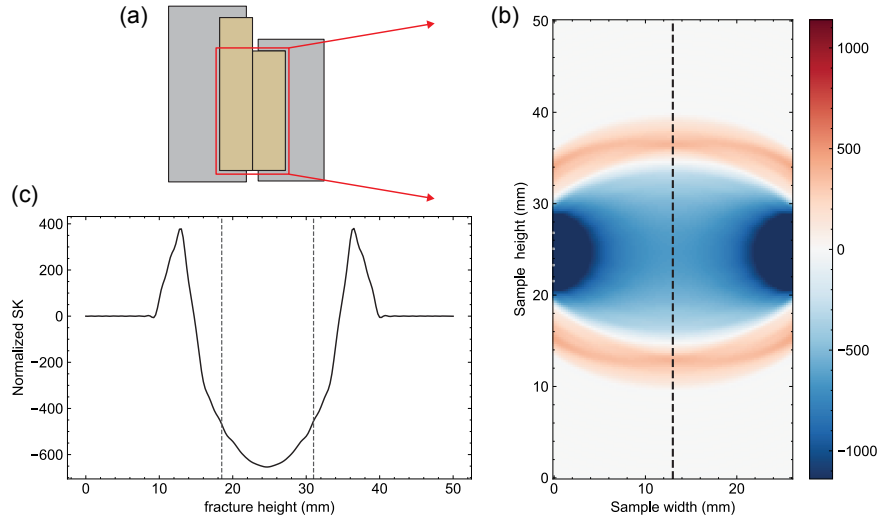
<sup>2</sup>Pennsylvania State University

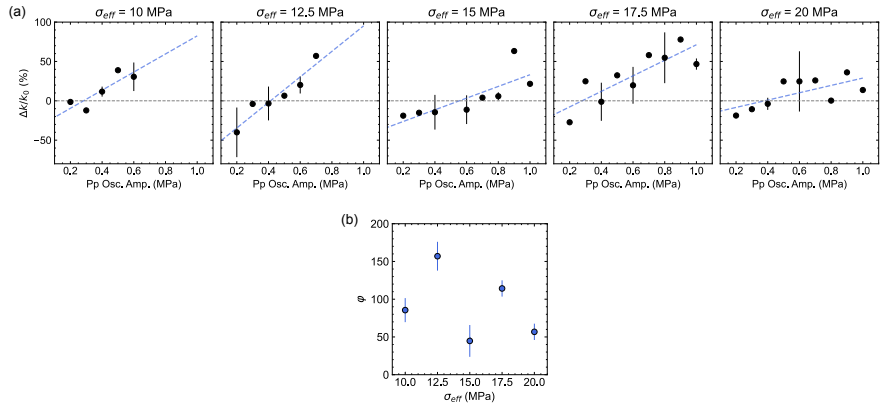
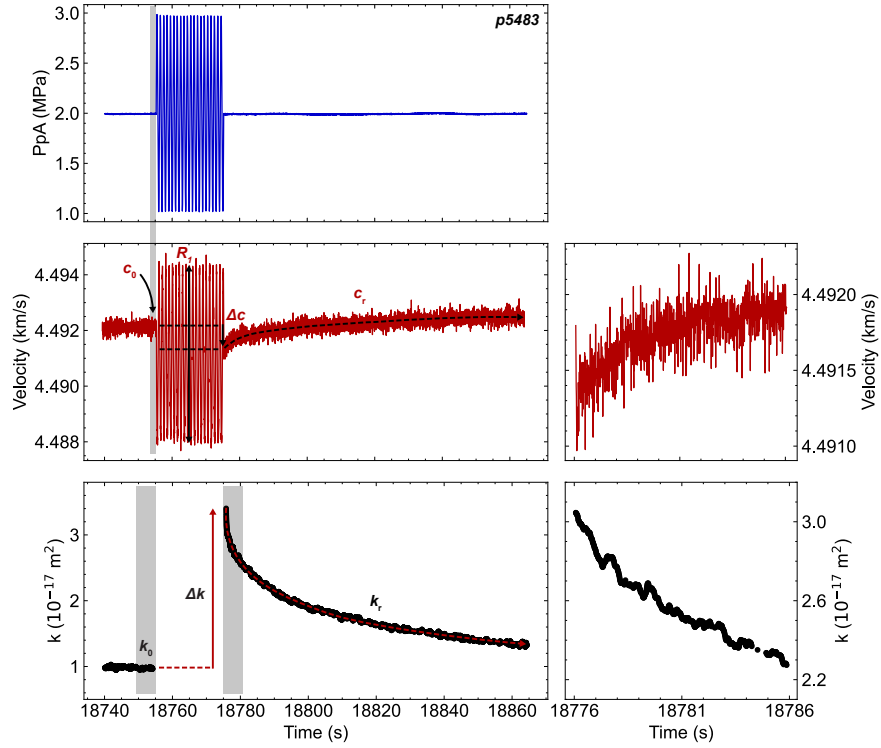
<sup>3</sup>Chevron

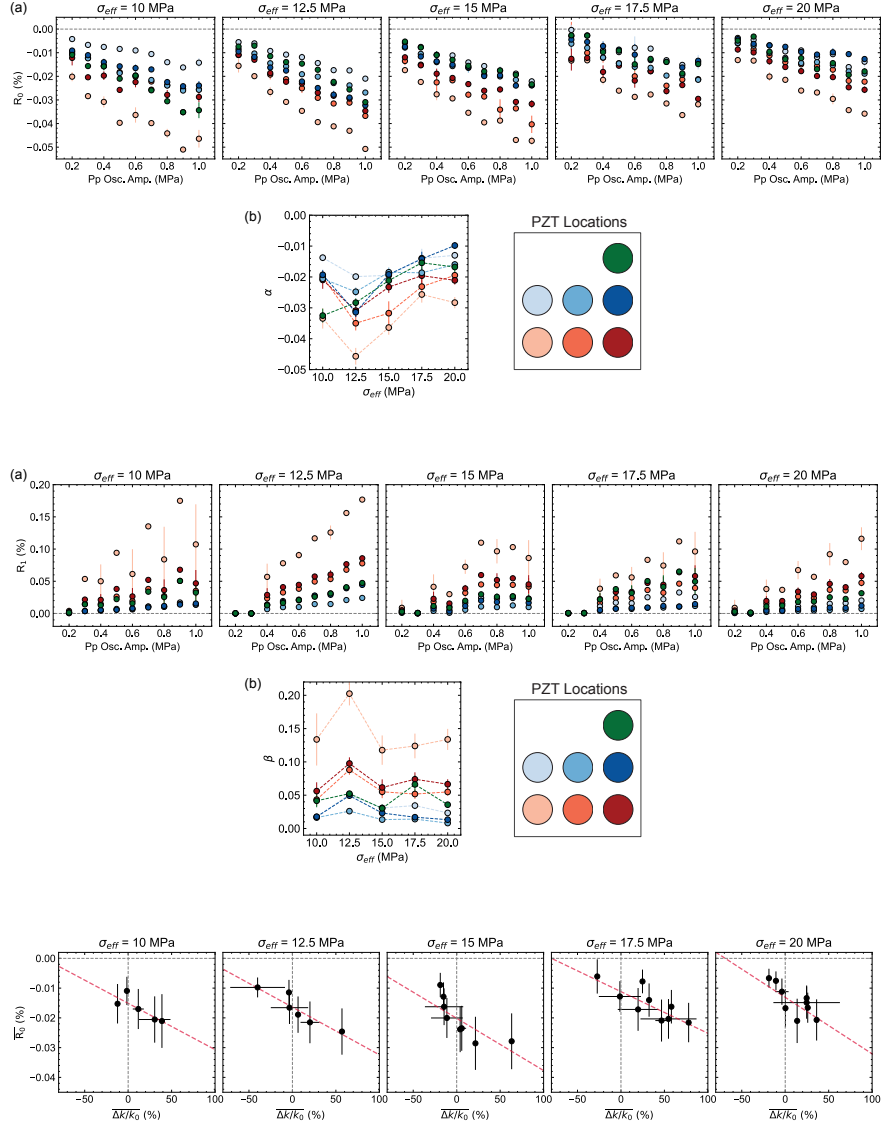
February 24, 2023

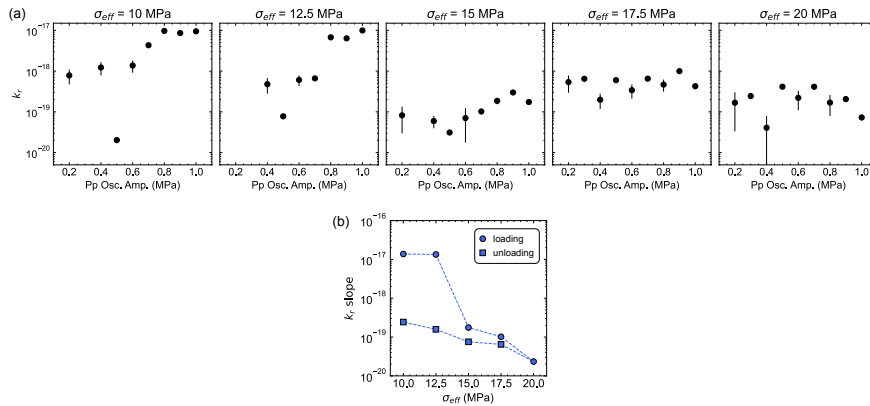
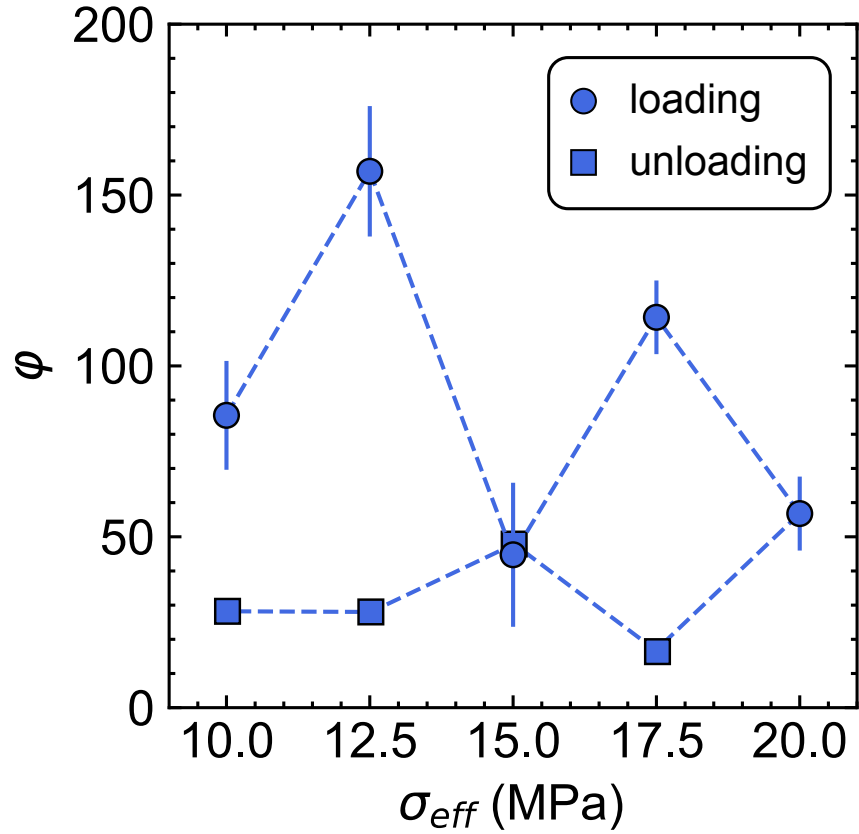
## Abstract

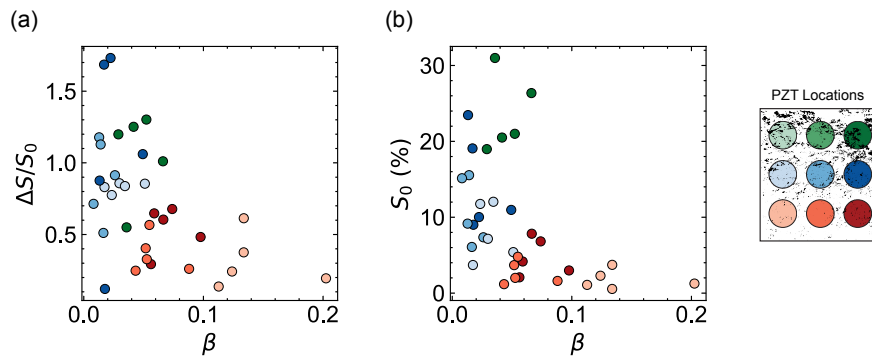
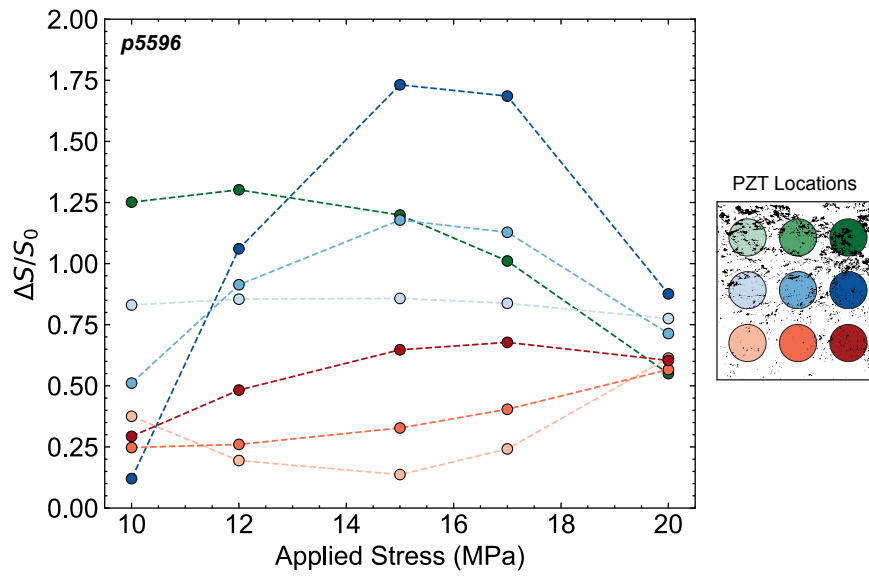
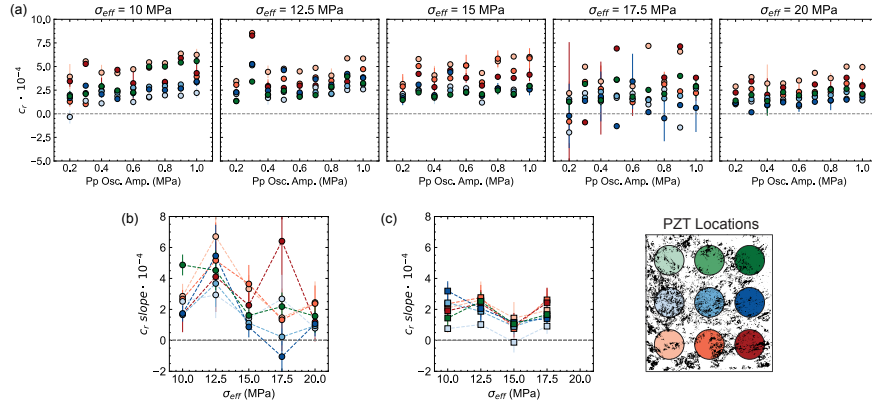
We exploit nonlinear elastodynamic properties of fractured rock to probe the micro-scale mechanics of fractures and understand the relation between fluid transport and fracture aperture and area, stiffness proxy, under dynamic stressing. Experiments are conducted on rough, tensile-fractured Westerly granite specimen subject to triaxial stresses. Fracture permeability is measured from steady-state fluid flow with deionized water. Pore pressure oscillations are applied at amplitudes ranging from 0.2 to 1 MPa at 1 Hz frequency. During dynamic stressing we transmit acoustic signals through the fracture using an array of piezoelectric transducers (PZTs) to monitor the evolution of fracture interface properties. We examine the influence of fracture aperture and contact area by conducting measurements at effective normal stresses of 10, 12.5, 15, 17.5, and 20 MPa. Additionally, the evolution of contact area with stress is characterized using pressure sensitive film. These experiments are conducted separately with the same fracture and they map contact area at stresses from 9 to 21 MPa. The resulting ‘true’ area of contact measurements made for the entire fracture surface and within the calculated PZT sensor footprints, numerical modeling of Fresnel zone. We compare the elastodynamic response of the the fracture using the stress-induced changes ultrasonic wave velocities for a range of transmitter-receiver pairs to image spatial variations in contact properties, which is informed by fracture contact area measurements. These measurements of the nonlinear elasticity are related to the fluid-flow, permeability, in response to dynamic stressing and similar comparisons are made for the slow-dynamics, recovery, of the fracture interface following the stress perturbations.

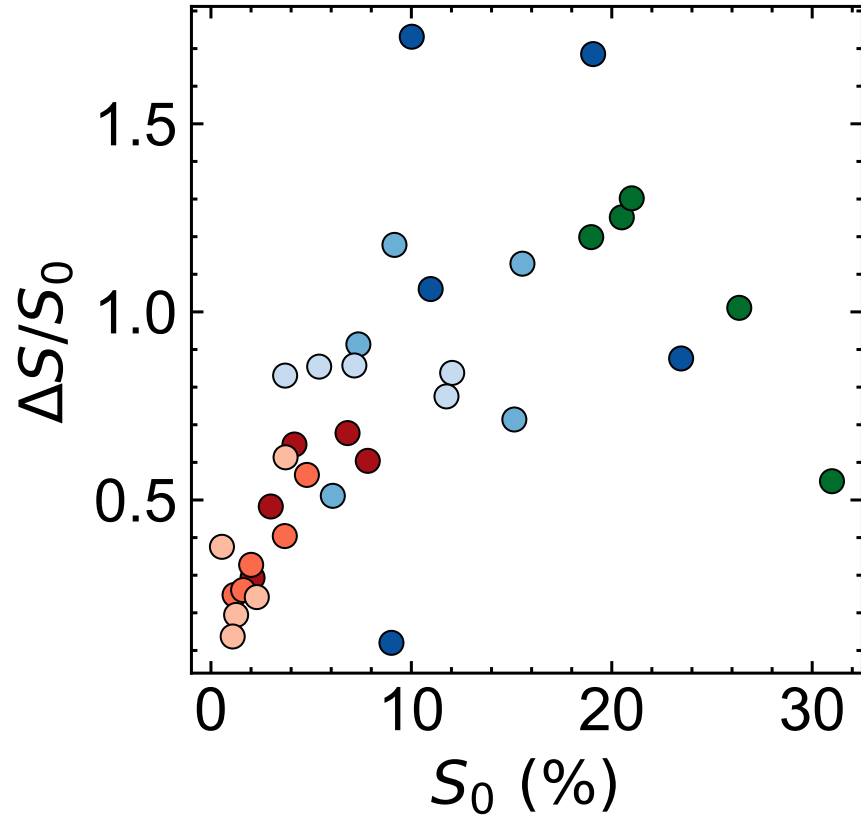


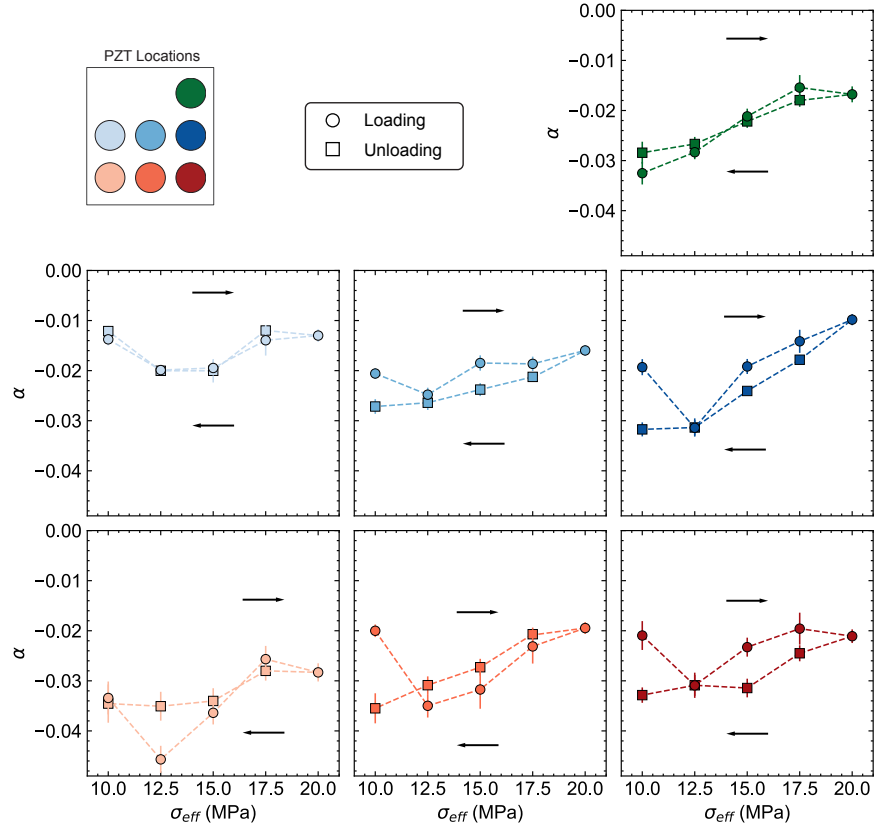


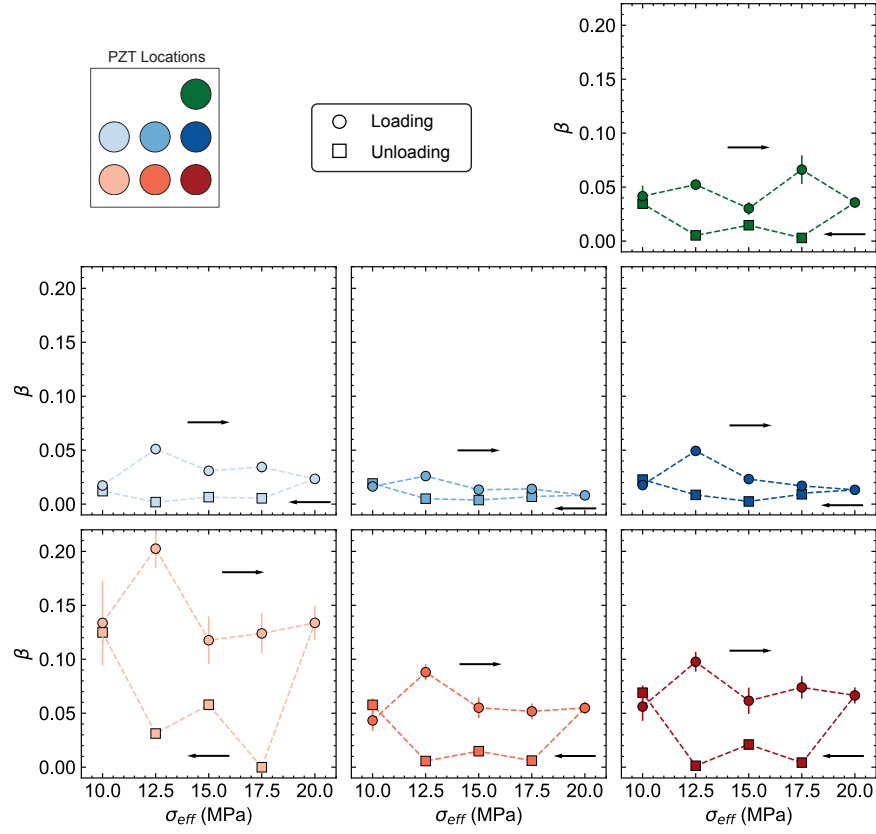


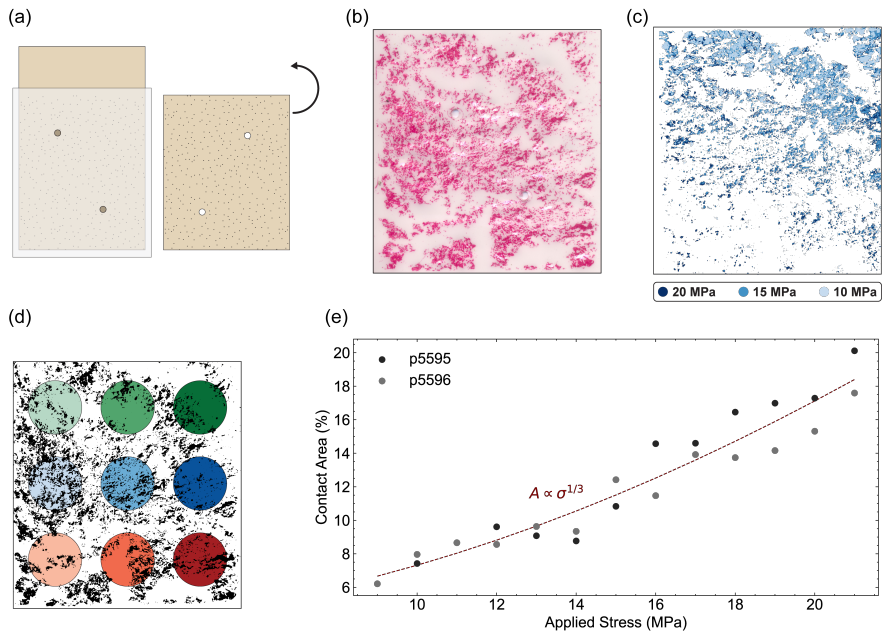
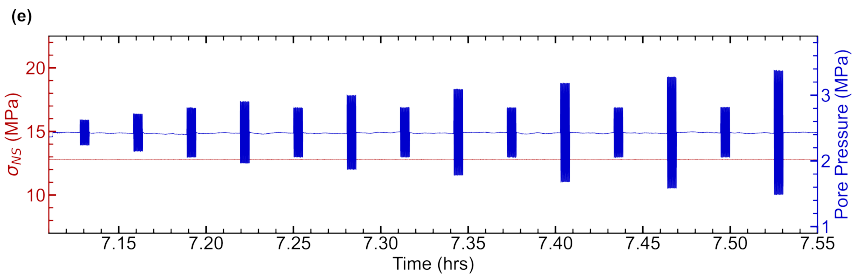
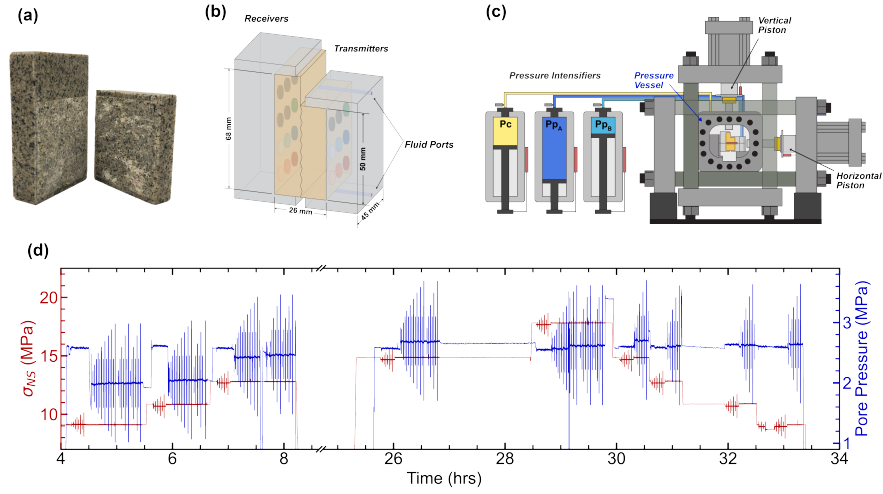












1                    **Relating hydro-mechanical and elastodynamic**  
2                    **properties of dynamically-stressed tensile-fractured**  
3                    **rock in relation to fracture aperture and contact area**

4                    **Clay E. Wood<sup>1</sup>, Prabhakaran Manogharan<sup>2</sup>, Andy Rathbun<sup>3</sup>, Jacques**  
5                    **Rivière<sup>2</sup>, Derek Elsworth<sup>4,1</sup>, Chris Marone<sup>1,5</sup>, Parisa Shokouhi<sup>2</sup>**

6                    <sup>1</sup>Dept. of Geosciences, Pennsylvania State University, University Park, PA 16802, USA

7                    <sup>2</sup>Dept. of Engineering Science and Mechanics, Pennsylvania State University, University Park, PA 16802,  
8                    USA

9                    <sup>3</sup>Chevron ETC, San Ramon, CA 12345, USA

10                    <sup>4</sup>Dept. of Energy and Mineral Engineering, EMS Energy Institute, and G3 Center, The Pennsylvania  
11                    State University, University Park, PA, USA

12                    <sup>5</sup>Dipartimento di Scienze della Terra, La Sapienza Università di Roma

13                    **Key Points:**

- 14                    • Lab experiments simulate conditions representative of fractures at various depths,  
15                    stresses, under dynamic stressing
- 16                    • Simultaneous measurements of fluid flow and active-source ultrasonic transmis-  
17                    sion show how these mechanisms are coupled
- 18                    • Local fracture aperture, not necessarily the stress state, dominate elastic and hy-  
19                    draulic responses to dynamic stressing

**Abstract**

We exploit nonlinear elastodynamic properties of fractured rock to probe the micro-scale mechanics of fractures and understand the relation between fluid transport and fracture aperture and area, stiffness proxy, under dynamic stressing. Experiments are conducted on rough, tensile-fractured Westerly granite specimen subject to triaxial stresses. Fracture permeability is measured from steady-state fluid flow with deionized water. Pore pressure oscillations are applied at amplitudes ranging from 0.2 to 1 MPa at 1 Hz frequency. During dynamic stressing we transmit acoustic signals through the fracture using an array of piezoelectric transducers (PZTs) to monitor the evolution of fracture interface properties. We examine the influence of fracture aperture and contact area by conducting measurements at effective normal stresses of 10, 12.5, 15, 17.5, and 20 MPa. Additionally, the evolution of contact area with stress is characterized using pressure sensitive film. These experiments are conducted separately with the same fracture and they map contact area at stresses from 9 to 21 MPa. The resulting ‘true’ area of contact measurements made for the entire fracture surface and within the calculated PZT sensor footprints, numerical modeling of Fresnel zone. We compare the elastodynamic response of the the fracture using the stress-induced changes ultrasonic wave velocities for a range of transmitter-receiver pairs to image spatial variations in contact properties, which is informed by fracture contact area measurements. These measurements of the nonlinear elasticity are related to the fluid-flow, permeability, in response to dynamic stressing and similar comparisons are made for the slow-dynamics, recovery, of the fracture interface following the stress perturbations.

## Plain Language Summary

We perform laboratory experiments with fractured rock to understand the relation between fluid flow, fracture openness, and elastic properties under oscillating stressing. These experiments are conducted on rough, pre-fractured granite specimens under stress conditions similar to those found in the shallow earth, a few kilometers in depth. Fluid pressure in the fracture is oscillated at various amplitudes at a fixed frequency. During this dynamic stressing, we use an ultrasonic device to monitor the evolution of the fracture interface. We examine the influence of fracture aperture and contact area by conducting measurements at increasing stress state. Additionally, the evolution of contact area with stress is characterized using pressure sensitive film, showing an image of where the two halves of the fracture are in contact. The ultrasonic monitoring reveals spatial variations in contact properties, which is informed by fracture contact area measurements. These measurements are also related to the fluid-flow in response to dynamic stressing and similar comparisons are made for how the fracture interface evolves, recovers, following the stress perturbations.

## 1 Introduction

During the course of industrial activities of hydrocarbon recovery or sequestration of carbon or wastewater (pumping, injection, and supercritical  $H_2O-CO_2$  fluids transport) are likely dominant factors in injection-induced seismicity (Healy et al., 1968; Raleigh et al., 1976; Simpson et al., 1988; Sminchak & Gupta, 2003; McNamara et al., 2015; McGarr et al., 2015; Walsh & Zoback, 2015). These industrial activities may produce dynamic perturbations in the local stress field of the subsurface, resulting in changes in poromechanical properties, potentially reactivating fault slip. The poromechanical response of faults, fractured rock, are similarly influenced by dynamic stressing from anthropogenic (industrial) and natural (elastic waves from earthquakes), indicating that these mechanisms – elastic softening and fluid transport – are correlated. In this work we seek to decouple the nonlinear elastic and fluid flow responses to dynamic stressing.

Field and laboratory observations demonstrate that elastic waves propagating from earthquakes may manifest transient changes of the elastic properties in fault zones. Observations from the field document a co-seismic softening, an instantaneous wave speed decrease, followed by a time-logarithmic post-seismic recovery of the fractured rock stiffness e.g., (Brenquier et al., 2008). Laboratory experiment implementing dynamic acousto-elastic testing (DAET) (Shokouhi et al., 2017), show that transmitted ultrasonic wave velocity decreases in response to stress oscillations followed by a time logarithmic recovery. Recently, DAET is used to study the nonlinear elastodynamic response of fractured rock under different stress and saturation conditions (Manogharan et al., 2021). In these studies, the nonlinear elastic responses can be activated with dynamic strains on the order of  $10^{-6}$  (Guyer & Johnson, 2009; Rivière et al., 2015). The nonlinear elastodynamic behavior of rock, intact or fractured, is modulated by minute features such as apertures (governing flow transport, asperity compliance) and higher-order effects such as nonlinear effective stiffness (impacted by rate and state-dependent friction and healing).

Dynamic strain perturbations propagating as elastic waves from earthquakes may induce pore pressure oscillations sufficiently large enough to change permeability (Brodsky & Lajoie, 2013). This may even perturb fault stability (Boettcher & Marone, 2004; Savage & Marone, 2007; P. A. Johnson et al., 2016) thus triggering seismicity (Brodsky & Lajoie, 2013; van der Elst et al., 2013). The underlying mechanism dominating empirical observations of permeability enhancement (and reduction) is postulated to be mobilizing and arresting of particles in porous media (Roberts, 2005; Roberts & Abdel-Fattah, 2009; Liu & Manga, 2009; Elkhoury et al., 2011; Candela et al., 2014, 2015). This effect of clogging and unclogging of pore throats has been observed experimentally (Elkhoury

et al., 2011; Candela et al., 2014), but the relation between these observations and elastic properties of fractured rock is not well understood.

Decoupling the hydro-mechanical and nonlinear elastodynamic properties of fractured rock is crucial for understanding consequences of dynamic stresses in the subsurface, especially at faults. Empirical studies, laboratory, investigating this relationship are currently limited to (Shokouhi et al., 2020; Wood et al., 2021). Here, we show results from complex laboratory experiments in which we combine the analysis of nonlinear elastodynamic and fluid transport data of a tensile-fractured specimen of Westerly granite subject to pore pressure perturbations. A unique contribution of this study is combining the aforementioned analysis with measurements of fracture asperity deformation including spatial variability.

## 2 Experimental Setup

We conducted a series of highly-constrained laboratory experiments on a pre-fractured sample of Westerly granite. For the first experiment (p5483), nonlinear elastic properties and flow rate were measured simultaneously under true triaxial stresses. In the following experiments (p5595 and p5596), the real area of contact on the fracture was estimated as a function of normal stress. The sample was cut into a L-shaped block 69 x 45 x 50 x 26 mm (Figure 1a-b) that we grooved along the perimeter and split in Mode I over a knife-edge to create a rough quasi-planar fracture. The pre-fractured sample was re-mated, placed between two loading platens, and then sealed with a latex membrane (separating pore fluid from confining fluid). The steel loading platens include embedded piezoelectric transducers (PZTs) as well as internal conduits to provide a distributed line source of fluid at both ends of the fracture, Figure 1b (using a modified version of the method of (Elkhoury et al., 2011)). After extensive preparation, the sample was placed inside a pressure vessel, Figure 1c-d. Each loading axis is independently servo-controlled, including upstream and downstream fluid flow from pressure intensifiers. Mechanical displacements and stresses are measured with direct current displacement transducers (Trans-Tek Series 240 DCDT) as well as custom-built load cells and recorded by a 24-bit analog-to-digital data acquisition system at 100 Hz. Active source ultrasonic monitoring was conducted using a Vantage<sup>TM</sup> Research Ultrasound (Verasonics) system and PZTs (APC International Ltd. 6.35 mm diameter compressional crystals) with a nominal center frequency of 500 kHz. The transmitting PZTs were pulsed every 0.2 ms and the ultrasonic response is recorded at the receiving PZTs at 25 MHz. A triggering signal from the Verasonics system is also recorded by the mechanical data acquisition system, allowing data synchronization. More details for the data acquisition are found in (Shokouhi et al., 2020; Manogharan et al., 2021; Wood et al., 2021).

Experiment	Description
p5483	Pp oscillation @ [10, 12.5, 15, 17.5, 20] MPa NS
p5595	Pressure sensitive film in horizontal configuration
p5596	Pressure sensitive film in vertical configuration

**Table 1.** Details of experiments used in this study.

### 2.1 Experimental Procedure

After sample preparation and installation into the pressure vessel, the experiment commenced with the application of a normal stress of  $\sim 10$  MPa followed by a confining pressure of  $\sim 5$  MPa. Next, the inlet ( $P_{pA} = 2.5$  MPa) and outlet ( $P_{pB} = 1.5$  MPa)

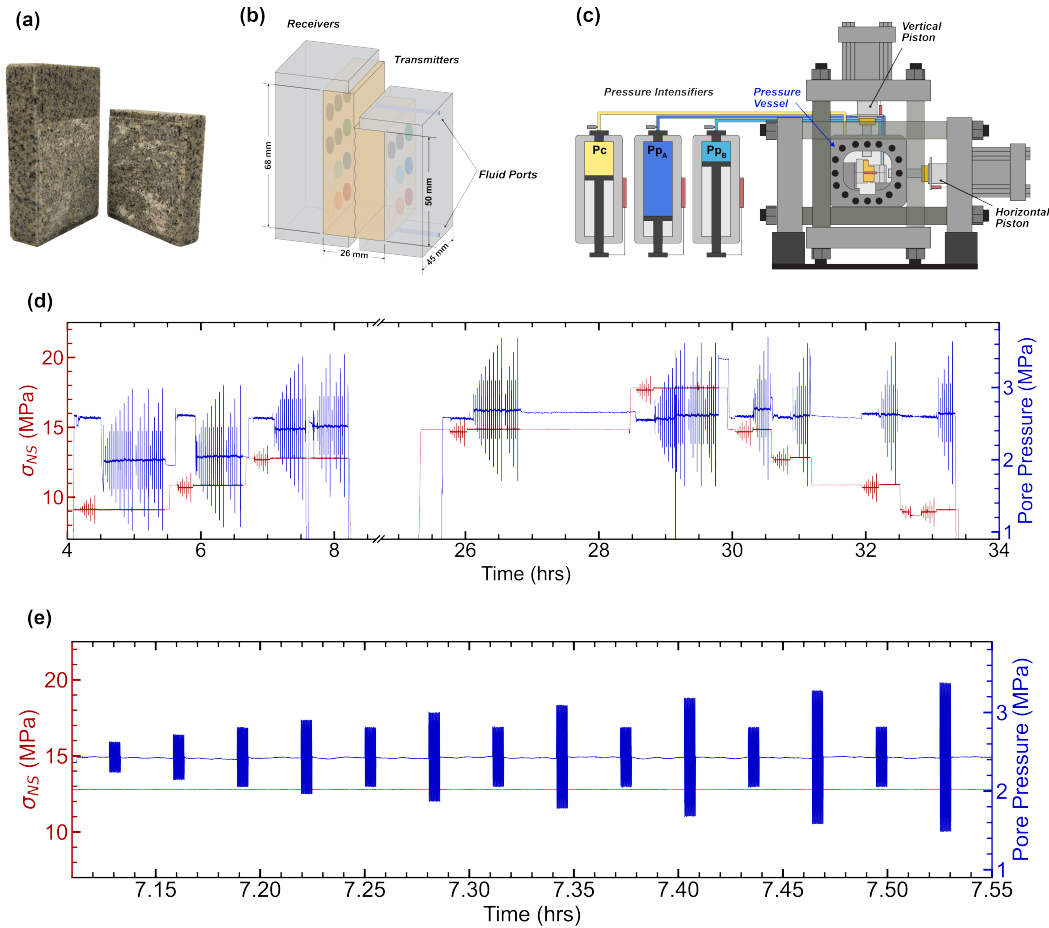


**Figure 1.** (a) Pre-fractured L-shaped Westerly granite sample. (b) Transmitter-receiver pairs used in active source ultrasonic monitoring embedded inside loading blocks (inactive sensors are dark-grey). (c) Biaxial loading apparatus with pressure vessel in Penn State's Rock Mechanics Laboratory. After the sample was prepared and installed in the pressure vessel, the fracture was saturated with deionized water. Imposed dynamic oscillations of pore pressure with amplitudes ranging from 0.2 to 1 MPa at 1 Hz. (d) Overview of the experiment showing the applied normal stress levels (10, 12.5, 15, 17.5, 20 MPa) in red and pore pressure oscillations in blue. (e) Pore pressure oscillations at 15 MPa  $\sigma_{\text{eff}}$ .

132 pressures were applied to provide a pressure differential across the sample, Figure 1. The  
 133 large difference in confining and pore fluid pressures prevents fluid from flowing around  
 134 the outside of the sample and/or along the grooved contour around the sample (used dur-  
 135 ing tensile fracture). Pore pressure oscillations were applied via servo control by feed-  
 136 ing a sinusoidal command signal to the inlet pressure intensifier  $P_{pA}$ .  $P_p$  stress oscilla-  
 137 tions ranged in amplitude from 0.2 to 1 MPa at 1 Hz while holding  $P_{pB}$  constant, Fig-  
 138 ure 1d. Afterward, the effective stress state was increased for a total of 5 different stress  
 139 levels [10, 12.5, 15, 17.5, 20] MPa. Due to experimental constraints, the effective stress  
 140 state was decreased to  $\sim 1$  MPa and held over several hours, before resuming the exper-  
 141 iment at 17.5 MPa. Three sets of pore pressure oscillations of varying amplitudes were  
 142 repeated three times at each normal stress level when stresses were incremented and four  
 143 sets when decremented, Figure 1d - e. The decremental stress levels, [17.5, 15, 12.5, 10] MPa,  
 144 were conducted in order immediately proceeding largest stress, 20 MPa, and with an hour

145 hold at 12.5 MPa. This protocol is designed to investigate the repeatability of measure-  
 146 ments and to determine the effect, if any, of loading and unloading on the fracture prop-  
 147 erties (elastic nonlinearity, permeability).

## 148 2.2 Permeability Measurement

149 Independent measurements of volumetric inflow ( $Q_A$ ) and outflow ( $Q_B$ ) rates are  
 150 made using Linear Variable Differential Transformers (LVDTs) attached to the pistons  
 151 of the pressure intensifiers. Our flow rate measurements are continuous, but we only con-  
 152 sider data for near-steady flow conditions ( $Q_A - Q_B \leq 5\%$ ). Darcy’s law is used to  
 153 calculate permeability  $k$ :

$$k = \frac{\mu L Q}{S \Delta P_P} \quad (1)$$

154 where  $Q = \frac{1}{2}(Q_A + Q_B)$  is the average flow rate,  $\mu$  is the fluid viscosity ( $10^{-3}$  Pa·s)  
 155 at 20° C,  $L$  is the length of the flow path along the fracture plane (50 mm) and  $S$  is the  
 156 cross-sectional area perpendicular to the flow path (45 mm × 26 mm), which includes  
 157 both the fracture and granite wall rock. This gives a bulk measure of permeability in-  
 158 cluding the fracture and surrounding rock matrix ( $k \sim 10^{-21}$  m<sup>2</sup>). The permeability  
 159 could also be calculated using other valid approaches (F. Zhang et al., 2017; Ishibashi  
 160 et al., 2018) which isolate the fracture permeability, but our focus here is on relative *changes*  
 161 in permeability dominated by the stress-sensitive fracture.

## 162 3 Active Source Ultrasonic Measurements

163 Active source ultrasonic data are continuously recorded before, during and after  
 164 the pore pressure oscillations. P-wave transmitting PZTs are excited with half-sine pulses  
 165 at 96 V having a center frequency of 500 kHz. Having an array of transmitters and re-  
 166 ceivers allows us to capture the spatial variability of the fracture’s elastodynamic prop-  
 167 erties (i.e., wave speed and amplitude). Various limitations prevented the use of all pos-  
 168 sible transmitter-receiver pairs; we report the results from 7 transmitter-receivers pairs.  
 169 The ultrasonic data are processed as previously documented (Rivière et al., 2013; Manogha-  
 170 ran et al., 2021; Wood et al., 2021), where all waveforms are cross-correlated with a re-  
 171 ference waveform (constructed by averaging 50 recorded waveforms at the beginning of  
 172 each experimental run before stress oscillations) to determine a time shift. Since the time  
 173 shift is typically smaller than the signals’ sampling time, often on the order of 1 ns, the  
 174 resolution is improved with a second-order polynomial fit to the peak of the cross-correlation  
 175 function. Absolute arrival time is obtained by adding the relative time shift to the p-  
 176 wave arrival time of the reference waveform (obtained using a threshold). To obtain (cor-  
 177 rected) p-wave wave speed, the corrected sample thickness (corrected for compaction/dilation  
 178 from internal DCDT) is divided by the absolute arrival times. The RMS amplitude is  
 179 calculated over an approximately 10  $\mu$ s time window including the p-wave arrival and  
 180 one full period of the waveforms.

### 181 3.1 Fresnel Zone Imaging

182 A key aim of this study is relating p-wave velocity and permeability changes to changes  
 183 in the fracture area. To accomplish this, we need to determine the size of the fractured  
 184 region probed by a given ultrasonic transmitter-receiver pair in our experimental con-  
 185 figuration. It is common to implement ray theory approximations of acoustic wave prop-  
 186 agation for active-source monitoring that connects changes in wave velocity and ampli-  
 187 tude to changes in experimental fault contact area (Hedayat et al., 2014; Shreedharan  
 188 et al., 2021), for example. In this approximation, waves propagating from source to re-  
 189 ceiver are considered to be in the high-frequency limit and thus the wavefield is collapsed  
 190 into a ray path approximated as an infinitesimally thin line (Spetzler & Snieder, 2004).  
 191 In reality, elastic waves propagate within a finite volume whose width is frequency-dependent,

192 rather than the volumeless trajectory of a ray path. The region around the propagation  
 193 trajectory responsible for diffraction in a medium is called the Fresnel zone or Fresnel  
 194 volume. The region around a ray that mostly influences the propagation of a band-limited  
 195 wave is called the first Fresnel zone. Previous studies estimated the ellipsoidal Fresnel  
 196 volume for active-source monitoring (Y. Zhang et al., 2015) by assuming point sources  
 197 for transmitters and receivers, which may underestimate the region or volume probed  
 198 by finite-sized transducers.

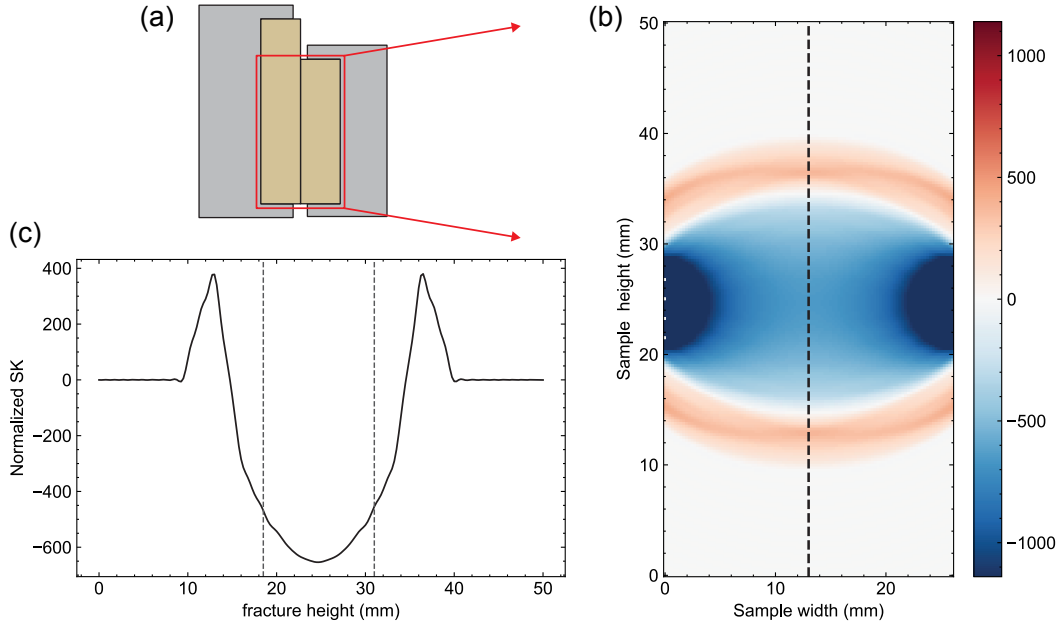


**Figure 2.** (a) Diagram of L-shaped configuration with region of interest outlined in red. (b) Amplitude sensitivity kernel model across granite block, where intensity represents response of transmitted wave to perturbation. (c) Profile of sensitivity kernel along the fracture plane (denoted by dashed black line in (b)). Dashed gray vertical lines indicate the half-power bandwidth of the Fresnel zone, where the transmitted waves are most sensitive to perturbations along the travel path (left to right).

199 Here, we numerically model the Fresnel zone resulting from our finite-sized transmitter-  
 200 receiver PZTs through the bulk rock sample using a sensitivity kernel (SK) to later es-  
 201 timate perturbations in the wavefield amplitude resulting from heterogeneities at the frac-  
 202 ture interface. The SK also provides insight on how other types of diffractors, i.e. wave  
 203 speed or density, affect acoustic wave propagation (Roux et al., 2013). The SK in Fig-  
 204 ure 2b shows the variation in transmitted wave field amplitude, where red colors indi-  
 205 cate increased amplitude and blue colors correspond to reduced relative amplitude (from  
 206 scattering). It is important to note that in our model we treat our transmitter and re-  
 207 ceiver as a collection of point sources and consequently the Fresnel zone is a superposi-  
 208 tion of their respective wavefields. The relative transmitted wave amplitude sensitiv-  
 209 ity kernel along the fracture profile is shown in Figure 2c, where the width of the half-  
 210 power bandwidth of the first Fresnel zone (blue) is delineated by dashed gray lines. For  
 211 a given transducer pair, we consider this region within the Fresnel zone to substantially  
 212 contribute to the recorded changes in transmission characteristics along the transmitter-  
 213 receiver travel path.

#### 214 **4 Fracture Contact Characterization**

215 After conducting the dynamic stressing experiment described above, we conducted  
216 two additional multi-step experiments to characterize the real area of contact for the ten-  
217 sile fracture specimen under load (p5595 and p5596, see Table 1). This was accomplished  
218 by inserting Fuji Prescale<sup>©</sup> Medium Film (1400 - 7100 psi) between the two halves of  
219 the fracture and loading the specimen to a range of stresses. The pressure sensitive film  
220 was removed and replaced after each step. Mating the fracture repeatably is imperative  
221 for the integrity of the asperities and also for accurate registration of contacts and voids.  
222 To that end, we installed locating pins to ensure that the fracture closed consistently each  
223 time and that the films were located precisely relative to one another. The pins were in-  
224 stalled by drilling two 1.588 mm diameter through-holes in the shorter sample half and  
225 blind holes in the taller half such that the locating pins could be inserted to ensure align-  
226 ment (Figure 3a). A blank pressure sensitive film was cut to size and then inserted be-  
227 tween the two fracture halves before loading to the desired target stress. This procedure  
228 was repeated with a new pressure sensitive film for each stress ranging from 9 to 21 MPa  
229 in increments of 1 MPa. Figure 3b depicts a representative pressure sensitive film loaded  
230 to 10 MPa; magenta color corresponds to regions of the fracture interface in contact and  
231 the remaining areas are void space. The pressure sensitive films are digitized using a Ep-  
232 son Perfection 3200 Photo color scanner at 3200 dpi resolution. Digitized scans are aligned  
233 using cross-correlation (with the lowest stress, 9 MPa, as the reference) and then bina-  
234 rized using an algorithm that generates a threshold value based on mean pixel intensity.  
235 Figure 3c show an overlay of the fracture contacts (shades of blue) for 10, 15, and 20 MPa  
236 (data from experiment p5596). Note that in experiment p5595, the sample was loaded  
237 horizontally, i.e., in the same configuration as in experiment p5483, whereas for exper-  
238 iment p5596, the entire setup was rotated 90° and the sample was loaded in the vertical  
239 direction. Loading the sample in the vertical direction greatly helped with properly align-  
240 ing the two halves of the sample.

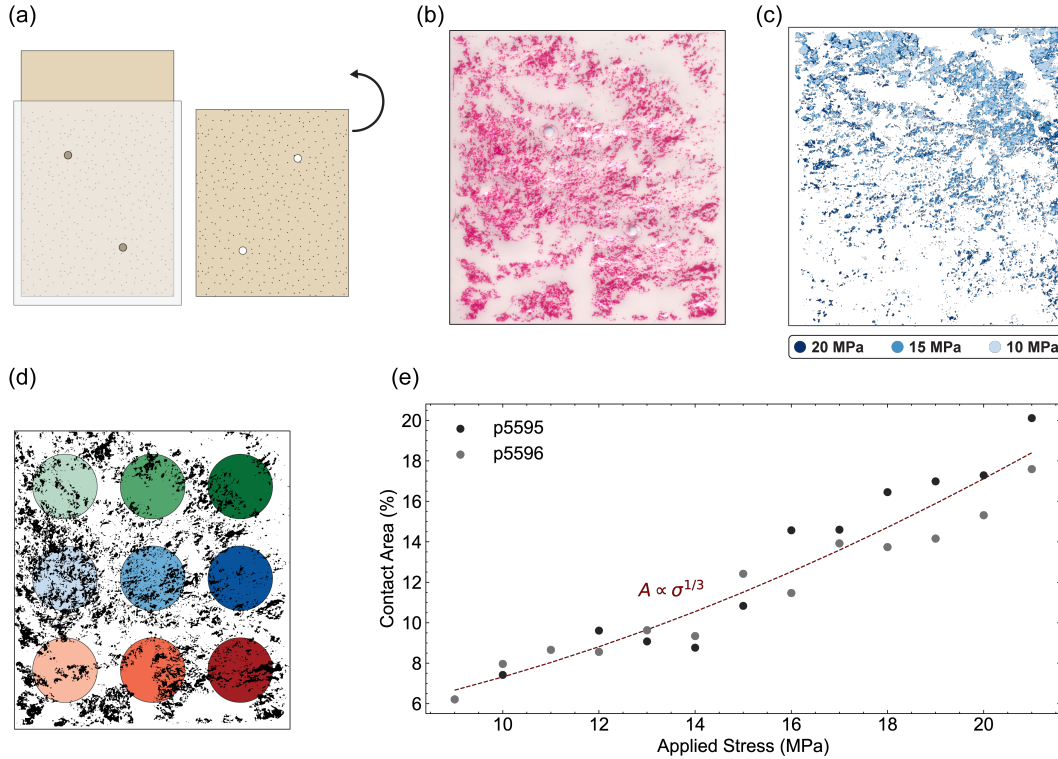


**Figure 3.** Integrating measurements of fracture contact area, aperture and elastic properties. (a) Sketch of fracture and locating pins to insert pressure sensitive film. (b) Example of pressure sensitive film after loading to 10 MPa (experiment p5596). Magenta regions represent contact and remaining areas are voids. (c) Superimposed images showing the evolution of contact area with applied stress at 10, 15, and 20 MPa. (d) Colored circles represent fracture regions probed by the array of transmitter-receiver pairs. The footprint size is recovered from the half-power bandwidth of the Fresnel zone. (e) Real contact area from film measurements (as in b) relative to nominal total area as a function of applied stress. The dashed line shows a cubic fit to these data, suggesting a Hertzian-contact relation between area and stress.

## 5 Results and Discussion

Our data include measurements of fracture permeability, p-wave velocity and amplitude as well as fracture contact area. The transducer array and pressure sensitive film provide information on the spatial variability of fracture properties and its evolution during dynamic stressing. We integrate that data with fluid flow measurements to develop a detailed understanding of fracture properties.

### 5.1 Connecting Sensor Footprint and Contact Area

A crucial component to this study is connecting fracture contacts to the active-source monitoring data. We estimate the real fracture contact area probed by each transmitter-receiver pair by superimposing the calculated PZT footprints (Section 3.1) onto the digitized and binarized pressure sensitive films. Figure 3d shows an example of fracture contacts (black indicates regions of contact and white indicates void) with locations and sizes of sensor footprints highlighted. This demonstrates the highly variable spatial distribution of contacts across the fracture. Additionally, the estimated total area of contact as

255 a function of applied stress is shown in Figure 3e. The dashed red line shows a cubic fit  
 256 to these data, suggesting a Hertzian-contact relation between real contact area (from pres-  
 257 sure sensitive films) and nominal applied stress (Hertz, 1881). Furthermore, we quan-  
 258 tify the change in real contact area within PZT footprints with stress, see Figure 4. As  
 259 expected, the contact area within each PZT footprint generally increases with stress with  
 260 a few exceptions, possibly due to the inevitable variations in mating of the two fracture  
 261 surfaces at each stress level. A comparison between the regions probed by sensors high-  
 262 lighted with dark green (top right) and light orange (bottom left) illustrate the dispar-  
 263 ity of contact area, especially for experiment p5596. The relation between these results  
 264 and nonlinear elastodynamic measurements are detailed in discussion section.

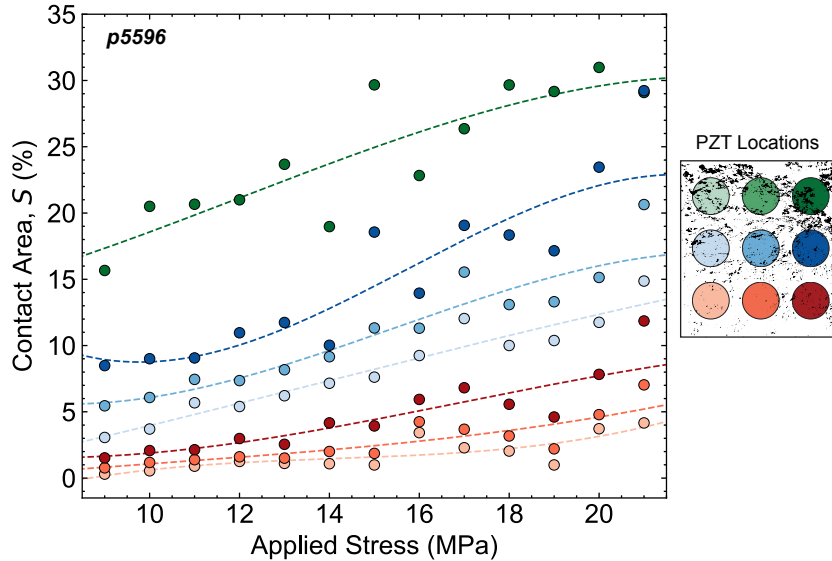


**Figure 4.** Percent area of fracture in contact within each PZT “footprint area” as a function of applied stress for one experiment. Contact area is directly estimated by pressure sensitive films at each stress. Note spatial variations in contact, as expected for a rough fracture, and also non-linear changes with stress. Each measurement involves re-mating the fracture and thus some variability is expected.

## 265 5.2 Hydraulic and Nonlinear Elastodynamic Responses

266 Rocks exhibit nonlinear elastic behavior due to the nonlinear response of their con-  
 267 stituent minerals and structures, viz. microcracks and compliant grain boundaries (Geyer  
 268 & Johnson, 2009; Rivière et al., 2015). When rocks are fractured, as in nature, this non-  
 269 linearity is compounded by contact acoustic nonlinearity at fractured interfaces. Figure  
 270 5 shows characteristic responses to dynamic pore fluid pressurization upstream (blue)  
 271 where transient softening and modulation of baseline velocity (P. Johnson & Sutin, 2005)  
 272 are manifest with slow recoveries to the pre-oscillation condition. In comparison, a lin-  
 273 ear elastic response would be effectively stress invariant, not showing any of the afore-  
 274 mentioned characteristics. Thus, nonlinear elasticity reveals much about the rock micro-  
 275 structure, fractures, and inter-grain contacts (Geyer & Johnson, 2009), all of which also  
 276 modulate the hydraulic properties. Both fluid and acoustic transmission characteristics  
 277 are highly sensitive to pore/fracture apertures and contact condition. Thus, we seek to  
 278 link the effect of stress state and resulting fracture aperture and contact to the elasto-  
 279 dynamic and hydraulic properties of dynamically-stressed fractured rock. The nonlin-  
 280 ear elastic response to dynamic stressing is characterized by the following: (1) relative

281 change in wave velocity,  $R_0$ , (2) the wave velocity amplitude modulation  $R_1$ , and (3) the  
 282 evolution of slow dynamics or post-oscillation recovery of wave velocity  $c_r$ . Both  $R_0$  and  
 283  $R_1$  are extracted using a projection procedure following (Rivière et al., 2013). The long-  
 284 term recovery, or slow dynamics, is observed to be logarithmic in time (Shokouhi et al.,  
 285 2017b, 2017a; Ten Cate and Shankland, 1996) and is recorded in a 90 s window follow-  
 286 ing each oscillation, although the time to full recovery may be much longer (Shokouhi  
 287 et al., 2017a). Besides the nonlinear elastodynamic measures described above, the relative  
 288 stress-induced change in permeability  $\Delta k/k_0$  and log-time recovery  $k_r$  are quan-  
 289 tified, as noted in the permeability subplot of Figure 5.

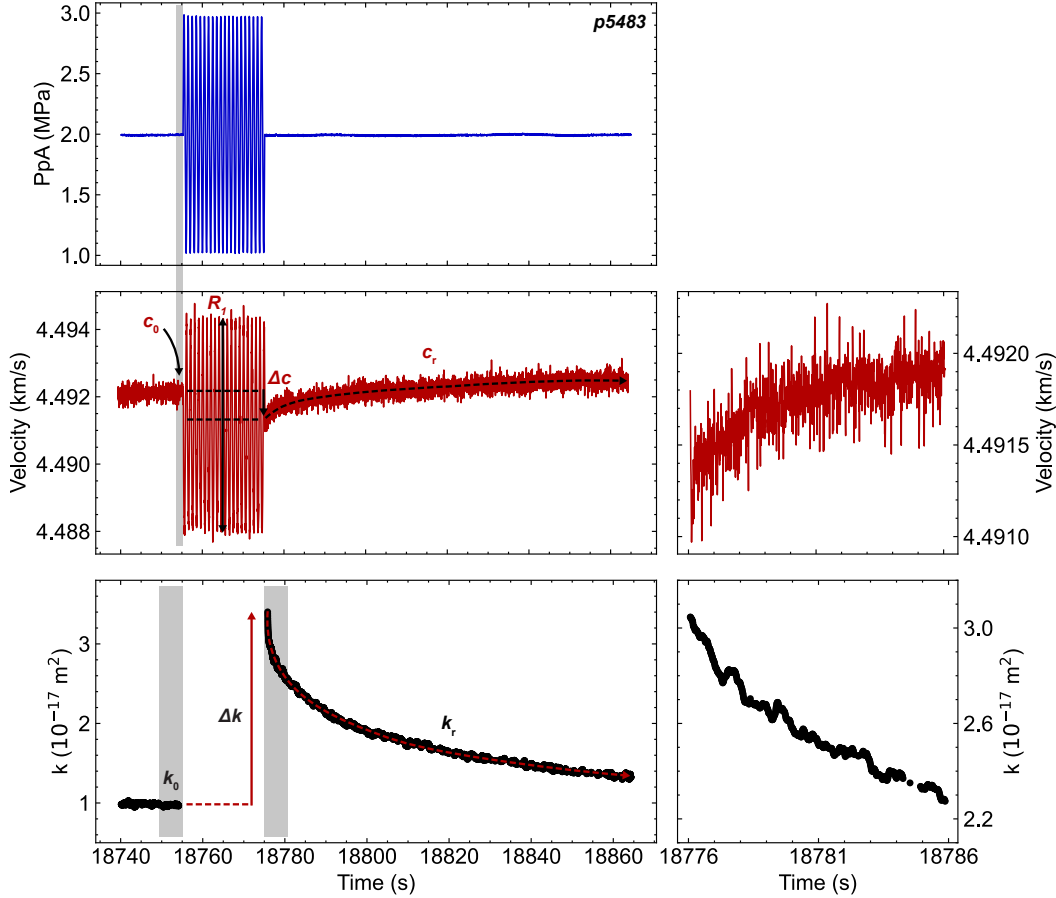


**Figure 5.** Excerpt of data from experiment p5483 illustrating the effect of pore pressure oscillation (1 MPa amplitude at 1 Hz) on ultrasonic p-wave velocity and permeability at applied normal stress of 20 MPa. A 1 second window preceding the oscillation is used to calculate the pre-oscillation values of velocity ( $c_0$ ). Relative changes in velocity ( $R_0 = \Delta c/c_0$ ) and wave velocity amplitude modulation ( $R_1$ ) are extracted from the projection procedure. Changes in permeability are calculated from pre-oscillation,  $k_0$ , and post-oscillation magnitudes,  $k_1$ , averaged in 5 s windows, respectively. Long-term post-oscillation evolution in wave velocity and permeability ( $c_r$ ,  $k_r$  respectively) are illustrated with arrows.

290

### 5.3 Dynamic Stress-induced Changes in Permeability

291

292

The relation between relative change in permeability ( $\Delta k/k_0$ ) and pore pressure ( $P_{pA}$ ) oscillation amplitude for each effective normal stress ( $\sigma_{\text{eff}}$ ) ranging from 10 MPa

293 to 20 MPa in 2.5 MPa increments is shown in Figure 6a. All oscillations were applied  
 294 with the same frequency of 1 Hz to allow direct comparison. As expected (Shokouhi et  
 295 al., 2020; Wood et al., 2021), we observe increasing permeability enhancement with in-  
 296 creasing amplitude of the applied pore pressure oscillation, though, in some cases this  
 297 reaches a plateau. Additionally, the scaling between  $\Delta k/k_0$  and oscillation amplitude (least-  
 298 squares fit) varies with the stress state of the fracture, generally decreasing with increas-  
 299 ing stress and assumed greater fracture closure, Figure 6b.

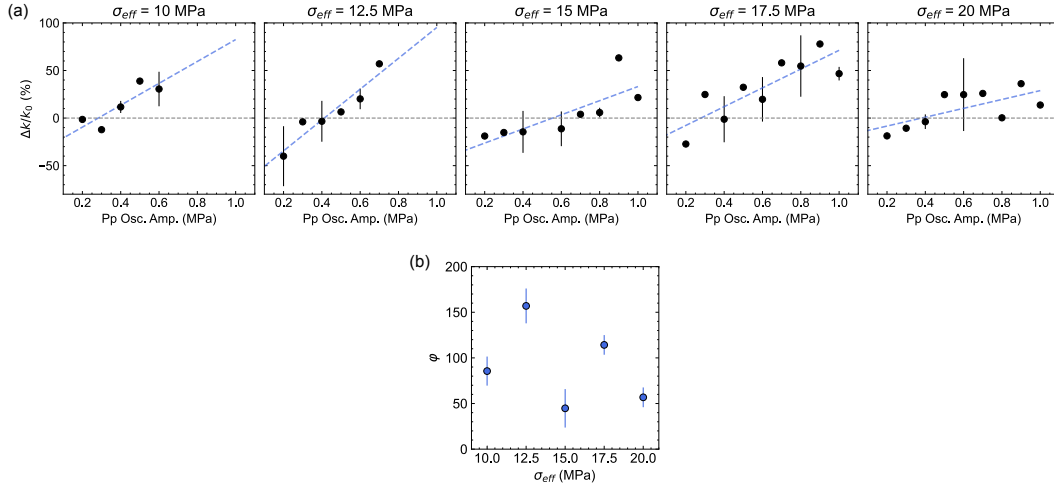


**Figure 6.** (a) Relative permeability change ( $\Delta k/k_0$ ) as a function of pressure oscillation amplitude for each applied normal stress. For all applied normal stresses, permeability changes increase with increasing pressure oscillation amplitude. Error bars are one standard deviation from mean for oscillations with repetitions. (b) The ratio of change in relative permeability with pore pressure amplitude,  $\varphi$ , generally decreases with an increase in effective stress.

#### 300 5.4 Dynamic Stress-induced Changes in P-wave Velocity

301 One of the measures of elastic nonlinearity, the relative change in velocity ( $R_0$ ) for  
 302 all transmitter-receiver pairs as a function of pore pressure oscillation amplitudes are shown  
 303 in Figure 7a. As noted previously (Manogharan et al., 2021; Wood et al., 2021), the mag-  
 304 nitude of  $R_0$  clearly increases with increasing pressure oscillation amplitude. Further-  
 305 more, after an initial increase, increasing effective stress generally reduces the magnitude  
 306 of  $R_0$ , as seen in Figure 7b in agreement with previous observations (Manogharan et al.,  
 307 2021; Rivière et al., 2016). The data in Figure 7 are colored by location of the PZTs along  
 308 the fracture plane (see scaled version in figure legend) to reveal the spatial variability  
 309 of the measured nonlinearity. One observations across all stress levels is that the nonlin-  
 310 earity (larger magnitude  $R_0$ ) measures the highest for the transducer pair at the bot-  
 311 tom left corner (light pink color). In contrast, the nonlinearity measured by the trans-  
 312 ducer pair at the top right corner (dark green color) is among the lowest at all stress lev-  
 313 els.

314 Another measure of elastodynamic nonlinearity that we investigate is the relative  
 315 change in the average amplitude of the wave velocity change,  $R_1$ . Figure 8a shows  $R_1$   
 316 as a function of pore pressure oscillation amplitude for all transmitter-receiver pairs. Like  
 317  $R_0$ , the average amplitude wave velocity  $R_1$  scales linearly with increasing pore pressure  
 318 oscillation amplitude, as expected (Rivière et al., 2015, 2013). As the fracture is clos-  
 319 ing with the increased applied stress, the slope of  $R_1$  with respect to the oscillation am-

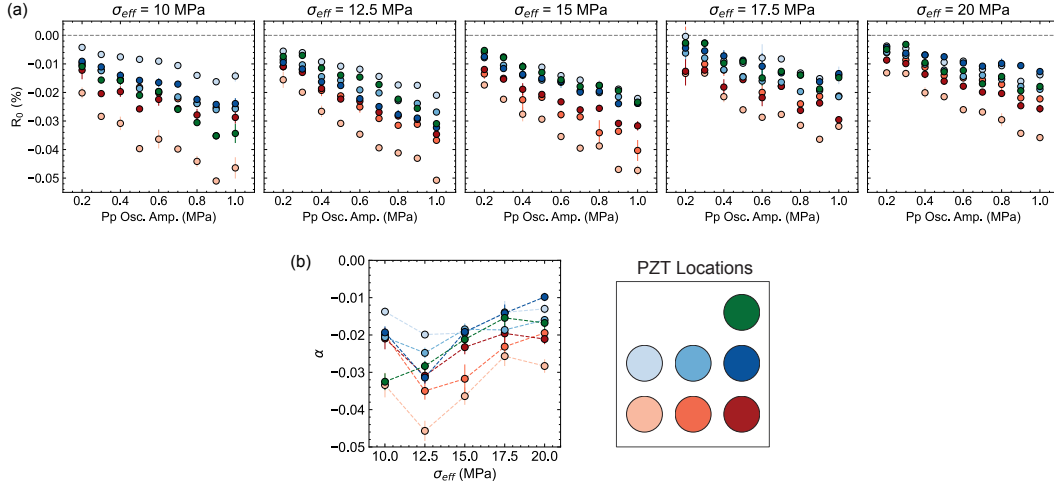


**Figure 7.** (a) Relative velocity change ( $R_0$ ) averaged over repetitions at each oscillation amplitude as a function of amplitude. Symbol colors correspond to the highlighted transducer footprint locations (see legend). (b) Slope of  $R_0$ ,  $\alpha$ , versus oscillation amplitude for each normal stress, a measure of hysteretic nonlinearity.  $\alpha$  decreases, then increases for most transmitter-receiver pairs. This represents a presumed fracture closure and increase in specific stiffness.

320  
321

plitude denoted as  $\beta$  increases at 12.5 MPa, decreases, and then slightly increases again at 17.5 MPa, see Figure 8b. The trend is slightly different for different transducer pairs.

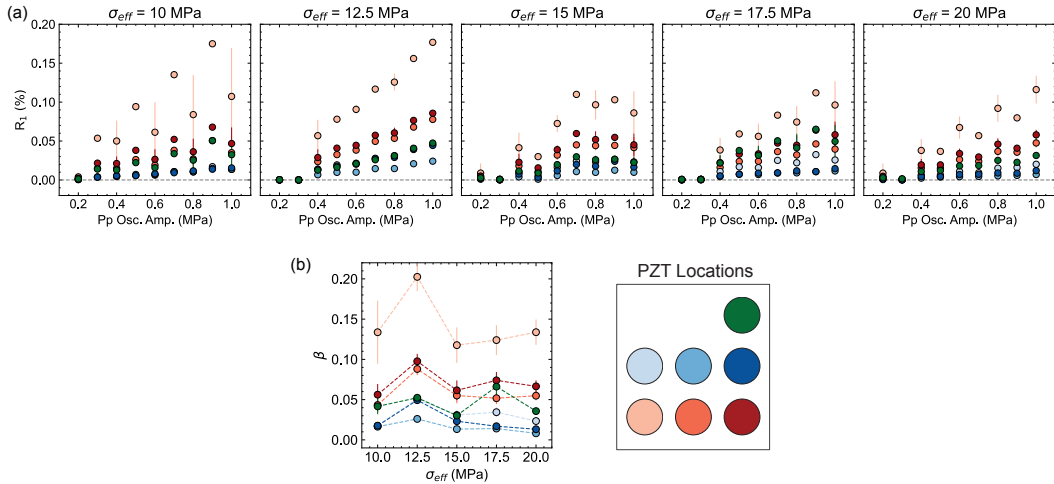


**Figure 8.** Relative change in the average amplitude of the wave velocity change ( $R_1$ ) as a function of pressure oscillation amplitude. Symbol colors correspond to various ray path locations across the fracture. (b) Slope of  $R_1$ ,  $\beta$ , versus pressure oscillation amplitude for increasing applied normal stress.

322

### 5.5 Linking Stress-Induced Elastodynamic and Hydraulic Changes

323  
324

To investigate the coupling between fluid flow changes and elastodynamic nonlinearity, we analyze how the observed stress-induced changes in p-wave velocity is connected

325 to changes in permeability at different normal stress levels. Figure 9 relates stress-induced  
 326 changes in p-wave velocity to changes in permeability ( $\Delta k/k_0$ ) for each effective applied  
 327 stress. In this figure,  $\overline{R_0}$  denotes  $R_0$  averaged over all transmitter-receiver pairs. Both  
 328 of these parameters measure average changes along the fracture in response to stress per-  
 329 turbations. We observe a linear correlation between  $\overline{R_0}$  and  $\Delta k/k_0$ , which appears to  
 330 be mostly independent of the stress level. This is observed from the slope of the dashed  
 331 red lines in Figure 9.

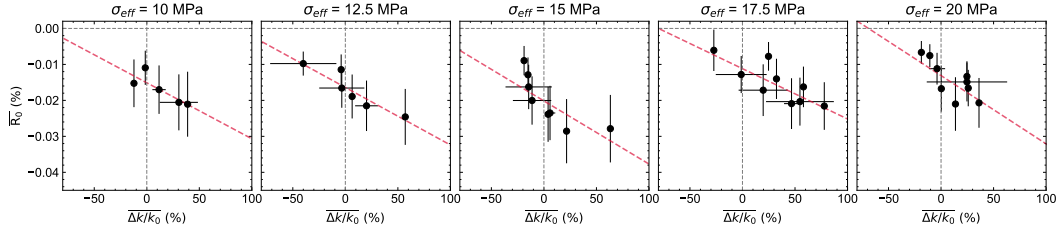


**Figure 9.** Relation between relative changes in velocity and permeability for each normal stress level.

## 332 5.6 Measurements during Loading vs. Unloading Phase

333 A key part of this study is understanding the effect of fracture aperture, degree to  
 334 which fracture is closed or open under different applied stresses, on the stiffness and hy-  
 335 draulic properties of the fracture interface. Besides measurements at increasing effective  
 336 stress levels (loading), we performed a subset of the pore pressure oscillation protocol  
 337 while unloading the sample. During the unloading phase, the confining stress was de-  
 338 creased incrementally to the stresses previously used during the loading phase (17.5, 15,  
 339 12.5, 10) MPa. Figure 10 shows summarized results of the  $\Delta k/k_0$  slope,  $\varphi$ , as a func-  
 340 tion of applied stress for both the loading (circle markers) and unloading (square mark-  
 341 ers) phases of experiment p5483. There is significant hysteresis comparing the loading  
 342 phase to the unloading phase with nearly an order of magnitude difference between  $\varphi$   
 343 at the beginning and end of the loading cycle. During unloading, the values of  $\varphi$  only  
 344 slightly increase. We posit that repeated stress oscillations and the large nominal stress  
 345  $\sigma_{\text{eff}} = 20$  MPa cause permanent, plastic deformation of the fracture asperities, and as  
 346 a result the preferred flow pathway(s) do not change significantly as the applied stress  
 347 is reduced.

348 This hysteresis is also observed in the measures of nonlinearity,  $R_0$  and  $R_1$  albeit  
 349 less pronounced. Figure 11 shows  $\alpha$  measured for each transmitter-receiver pair as a func-  
 350 tion of applied stress for the loading and unloading phases of experiment p5483. Dur-  
 351 ing the loading phase, there is a characteristic decrease at  $\sigma_{\text{eff}} = 12.5$  MPa (higher non-  
 352 linearity) and then an increase at  $\sigma_{\text{eff}} = 20$  MPa (lower nonlinearity) for most of the  
 353 transducer pairs. However, during the unloading phase, the change in  $\alpha$  is either nearly  
 354 invariant with applied stress (light blue, dark red) or linearly increases in magnitude. A  
 355 common observation across all transducer pairs is the slightly higher measured nonlin-  
 356 earity during unloading than that during the loading phase at a given stress. Possibly,  
 357 the asperities break and deform when loading leading to a larger instantaneous stress-  
 358 induced stiffness change  $R_0$  during unloading and therefore, larger  $\alpha$  magnitudes. Sim-  
 359 ilarly, Figure 12 shows  $\beta$  as a function of applied stress for each transmitter-receiver pair  
 360 during the loading and unloading phases of the experiment. The measured  $\beta$  and hys-  
 361 teresis vary significantly for different transducers. The pairs in the two upper rows with  
 362  $\beta$  close to zero show nearly stress-invariant wave velocity amplitude modulation, whereas  
 363 others in the bottom row show greater nonlinearity and hysteresis loops. As previously

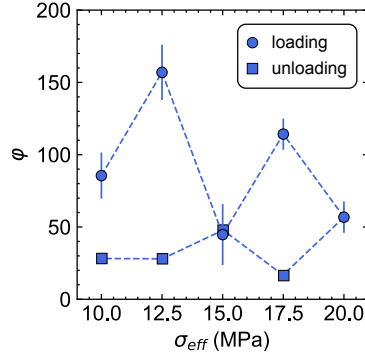


**Figure 10.** Slope of  $\Delta k/k_0$ ,  $\phi$ , as a function of applied stress for loading and unloading phases of the experiment. There is noticeable hysteresis during the unloading phase, where the lowest applied stress differs by an order of magnitude.

364 noted, the measured  $\beta$  during the loading phase is mostly insensitive to the effective stress  
 365 level except for a local increase at 12.5 and a slight increase at 17.5 MPa for some trans-  
 366 ducer pairs. During the unloading phase,  $\beta$  generally increases returning to the initial  
 367 value measured at 10 MPa. The observed hysteresis loops appear larger for transducer  
 368 pairs with a larger measured  $\beta$ . Unlike what is observed for  $\alpha$ ,  $\beta$  measures consistently  
 369 lower during unloading than loading. Previous studies relate  $\beta$  to opening and closing  
 370 of fractures (Rivière et al., 2015). We hypothesize that the broken and deformed frac-  
 371 ture asperities during loading facilitate the mating of the two fracture surfaces making  
 372 it harder for the fracture and close thus smaller  $\beta$ . We note that for both  $\alpha$  and  $\beta$ , the  
 373 nonlinearity measured during unloading increases with decreasing stress, which is expected  
 374 due to fracture opening.

### 375 5.7 Permeability Recovery and Slow Dynamics

376 The post-oscillation evolution of permeability and p-wave velocity is related to how  
 377 the fracture contact asperities have been transiently or irreversibly changed during the  
 378 imposed oscillations. Also, the time-dependent phenomenon provides an indication of  
 379 the rate of healing and recovery at the perturbed interface. Here, this is measured as the  
 380 slope of the recovery in logarithmic time. Our observations indicate that log-time per-  
 381 meability recovery  $k_r$  is mostly invariant to the amplitude of pore pressure oscillations  
 382 at higher normal stresses ( $> 12.5$  MPa), Figure 13a. At lower normal stresses, the log-  
 383 time evolution recovers more quickly at lower pore pressure oscillation amplitudes. These  
 384 overall trends are summarized in Figure 13b with the slope of  $k_r$  as a function of applied  
 385 stress, which also includes results from the unloading phase of the experiment.

386 The p-wave velocity recovery  $c_r$  for all transmitter-receiver pairs as a function of  
 387 pore pressure oscillation amplitude is shown in Figure 14a. The measured recovery rate  
 388 slightly increases with increasing pressure oscillation amplitude i.e., the wave velocity  
 389 returns to the pre-oscillation value quicker after larger amplitude oscillations. The slopes  
 390 change slightly and unsystematically with fracture closure, Figure 14b, but during the  
 391 unloading phase, there is much less spread between the transmitter-receiver pairs and  
 392 more systematic evolution with applied stress (fracture opening). In Figures 13b and 14b  
 393 and 14c, both  $k_r$  and  $c_r$  slopes show a hysteretic relationship with fracture closing and  
 394 opening (increasing and decreasing applied stress).

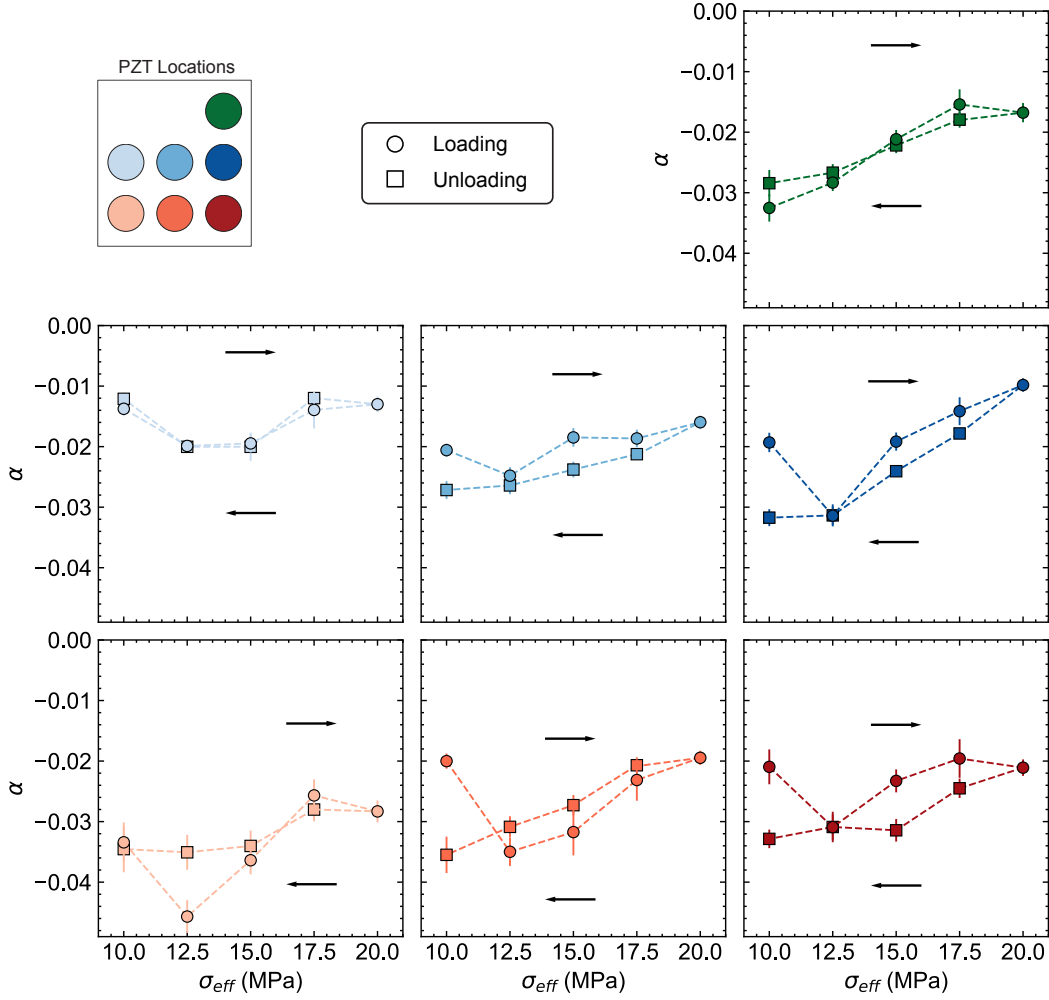


**Figure 11.**  $\alpha$  vs. applied stress for loading and unloading phases of the experiment. A lower value of  $\alpha$  corresponds to a larger nonlinearity. We see an overall decrease in nonlinearity with applied stress ( $\alpha$  tends toward zero) for some of the pairs (e.g., dark green), while no clear trend can be seen for other pairs (i.e., light blue).

395

### 5.8 Relating Contact Area to Elastodynamic Properties

396

397

398

399

400

401

402

403

404

405

406

407

True fracture contact area constrain many of the elastodynamic and hydraulic observations. Figure 3c,e show that the estimated true contact area using pressure sensitive film increases as a function of applied stress in a Hertzian-contact-like manner (cubic relationship), effectively reducing aperture and enlarging individual contact areas. Defining Fresnel ray-path tunnels between transmitters and receivers (PZT footprints) projected on the pressure sensitive film images allows us to investigate the true contact area and its evolution for individual transducer pairs. Figure 4 confirms significant heterogeneity in the area of contact for various transmitter-receiver pairs at the same applied stress. We posit that this heterogeneous distribution in asperity contact resulting in spatial variation of specific stiffness across the fracture is a key factor behind the observed differences among nonlinear elastodynamic measurements from different transducer pairs.

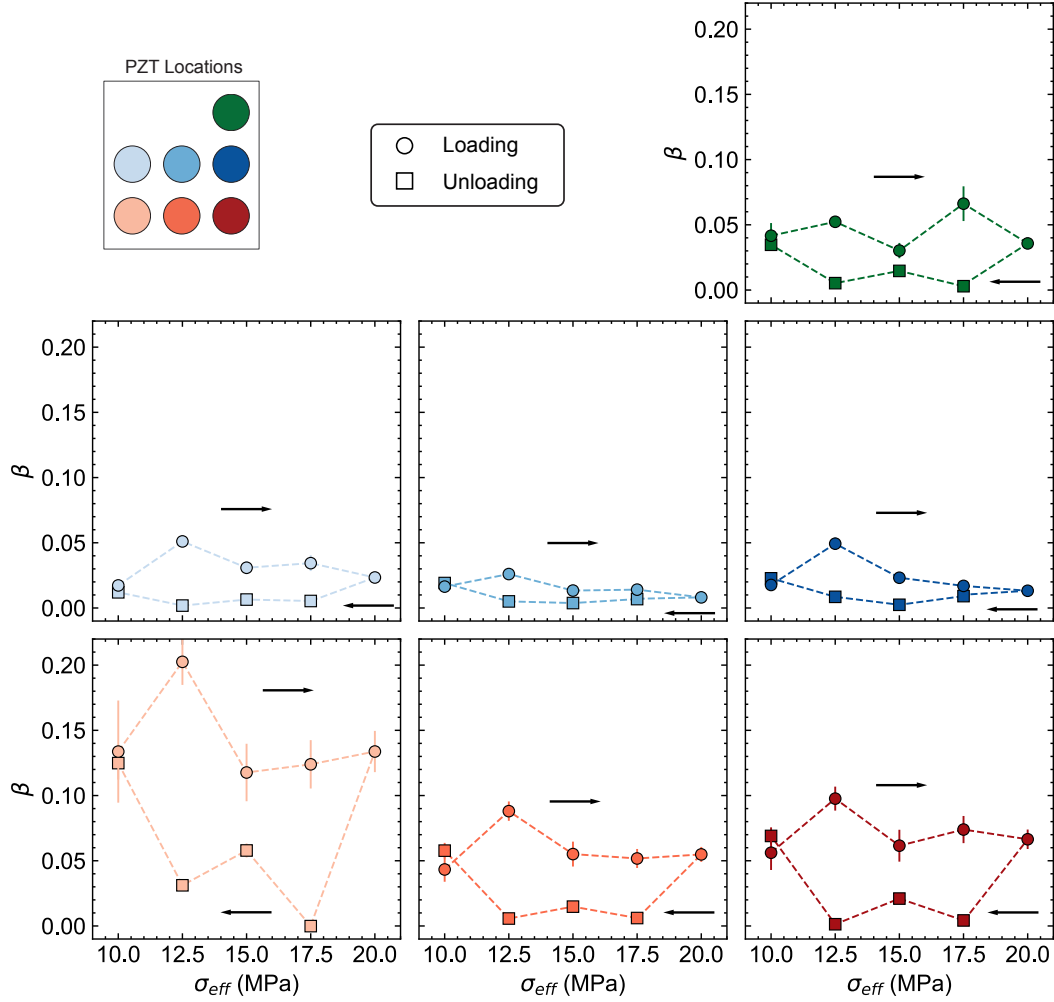


**Figure 12.**  $\beta$  vs. applied stress for loading and unloading phases of the experiment.

408 Next, we investigate the relationship between the nonlinear parameters and esti-  
 409 mated contact area. Since stiffness is defined as  $K = \frac{F}{S\delta}$ , where  $\delta$  is displacement, as-  
 410 suming a nominal unit area and considering the dependence of the contact force  $F$  on  
 411 the number and radii of asperities in contact (Jin et al., 2020), we may take contact  $S_0$   
 412 area to be a proxy for the interface stiffness at rest  $K_0$ . In other words, a fracture with  
 413 a larger true contact area is expected to be stiffer. Similarly, the change in contact area  
 414 due to dynamic stressing  $\Delta S/S_0$  is expected to correlate with the change in stiffness  $\Delta K/K_0$   
 415 and in turn with change in wave speed, the elastodynamic nonlinearity. Figure 15 shows  
 416 the relative change in contact area ( $\Delta S/S_0$ ) for each transmitter-receiver pair as a func-  
 417 tion of applied stress.  $S_0$  is the contact area at each applied normal stress used in ex-  
 418 periment p5483 ([10, 12.5, 15, 17.5, 20] MPa) and  $\Delta S$  is the slope from a linear fit to  
 419 the contact area  $\pm 1$  MPa at each stress level (for example, at 15 MPa, contact area ob-  
 420 tained at 14, 15 and 16 MPa is used, see Figure 4). In the data from experiment p5596,  
 421 most of the transmitter-receiver pairs follow a similar trend showing a modest increase  
 422 in  $\Delta S/S_0$  at 12 MPa, then a decrease at 17.5 MPa, followed by an increase at 20 MPa.

423 Since the nonlinearity parameter  $R_1$  is believed to be related to the opening/closing  
 424 of the fracture, it is considered to be a measure of  $\Delta K/K_0$ . Therefore, an important ques-  
 425 tion to ask is whether our data show a correlation between  $R_1$  and  $S_0$  or  $\Delta S/S_0$ . To our

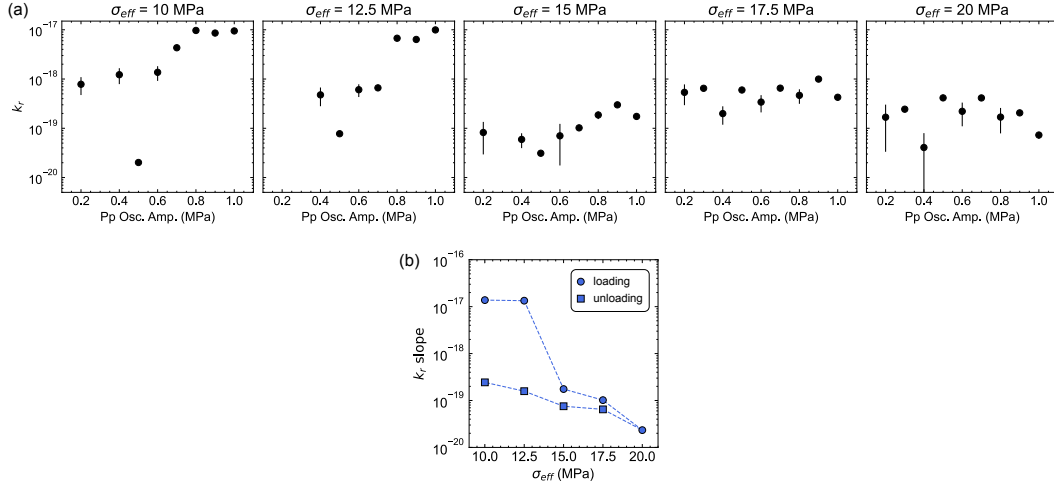


**Figure 13.** (a) Log-time recovery of permeability after pressure oscillations for each normal stress. The recovery rate is oscillation amplitude-dependent at lower stresses ( $< 15$  MPa), but not at higher normal stresses ( $> 12.5$  MPa) and with relatively little change up to the largest normal stress (20 MPa). (b) Slopes of  $k_r$  as a function of applied stress for the loading (black markers) and unloading (grey markers) phases of the experiment.

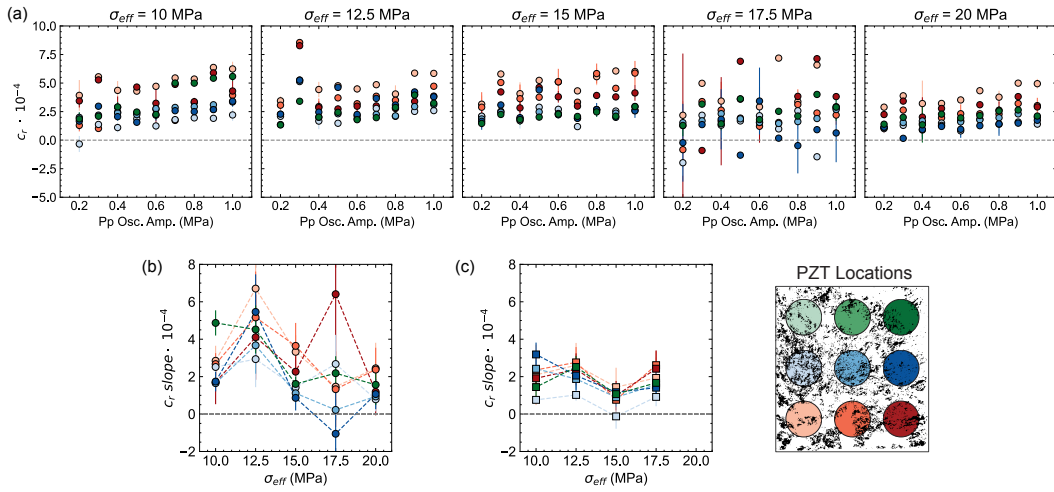


**Figure 14.** (a) Log-time recovery rate for all transmitter-receiver pairs. Positive values indicate a transient change to the fracture asperities and negative values indicate irreversible changes to fracture contacts. (b) The slope of  $c_r$  as a function of applied stress does not seem to systematically evolve with increasing  $\sigma_{eff}$ . (c) Slopes of  $c_r$  as a function of applied stress during the unloading phase of the experiment.

426 knowledge, this is the first experimental investigation of the relation between contact area  
 427 and elastic nonlinearity of a fracture. The expectation is that regions of the fracture with  
 428 a larger true contact area  $S_0$  be stiffer and therefore, harder to open and close (at a given  
 429 dynamic stress level); therefore, having a smaller  $S_0$  is  $R_1$  or  $\beta$ . This reasoning is sup-  
 430 ported by our observations shown in Figure 16. Following the same line of reasoning, one  
 431 may expect a positive correlation between  $\beta$  and normalized change in area  $\Delta S/S_0$ . We  
 432 attempt to investigate this relation in Figure 16, which shows  $\Delta S/S_0$  as a function of

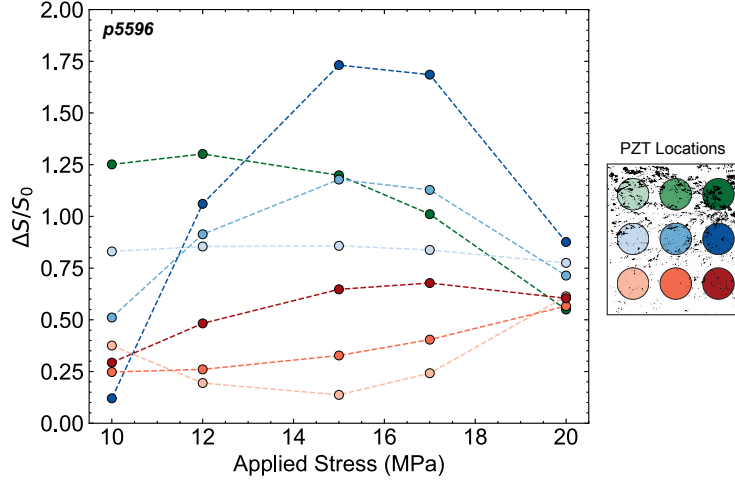


**Figure 15.** Relative change in contact area  $\Delta S/S_0$  for each PZT pair as a function of applied stress for experiments p5595 and p5596. Most receivers (p5596) show a modest increase in  $\Delta S/S_0$ , then a decrease at 17.5 MPa, followed by an increase at 20 MPa.

433  $\beta$  for all transmitter-receiver pairs, where we observe a negative correlation between the  
 434 two quantities albeit with a lot of scatter. Figure 17 shows plot of  $\Delta S/S_0$  vs  $S_0$  reveals  
 435 that the relative change in contact area generally increases with increasing contact area,  
 436 which is counter-intuitive. This could be a result of errors in estimating  $\Delta S$ , which re-  
 437 lies on comparing the estimated contact areas at two different (but close) stress levels  
 438 from two separate experiments.

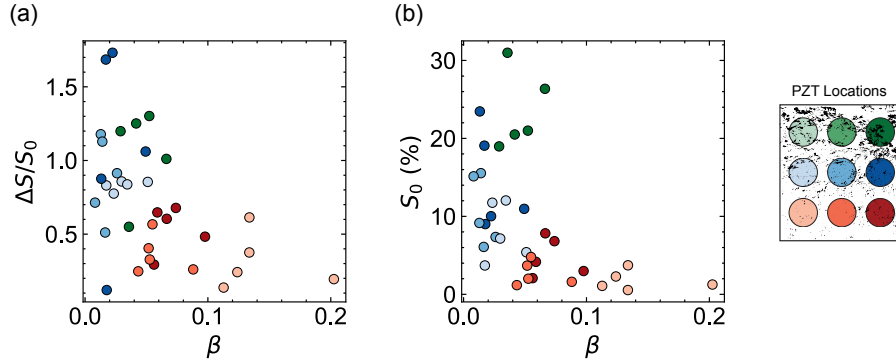


**Figure 16.** (a) Regions with larger contact area ( $S_0$ ) exhibit smaller measure of nonlinearity,  $\beta$ , and regions with small  $S_0$  exhibit larger nonlinearity. (b) Contact area change  $\Delta S/S_0$  from experiment p5596 as a function of  $\beta$  for all transmitter-receiver pairs.

## 6 Conclusion

439

440 We present tightly-constrained experiments to investigate the role of aperture and  
 441 real contact area on hydraulic and elastodynamic properties of dynamically-stressed frac-  
 442 tured rock. Conditions are representative of fractures at various depths and therefore  
 443 stresses. Simultaneous measurements of fluid flow and active-source ultrasonic transmis-

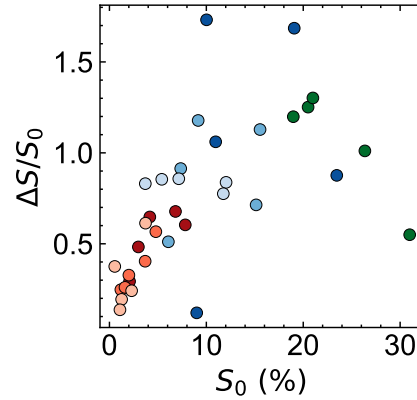


**Figure 17.** Comparison between contact area change  $\Delta S/S_0$  and nominal contact area,  $S_0$ , for respective transmitter-receiver pairs. This reveals a counter-intuitive relation that the relative change in contact area generally increases with increasing contact area.

444 sion show how these mechanisms are coupled – potentially linking permeabilities with  
 445 elastodynamic characteristics. Additionally, we quantify the heterogeneity of the frac-  
 446 ture contacts at discrete stresses in order to better interpret our observations from mul-  
 447 tiple transducer pairs probing different parts of the fracture.

448 Fractured Westerly granite exhibits characteristic mesoscopic elastic nonlinearity  
 449 when subjected to pore pressure oscillations, revealing rich information about the con-  
 450 tact mechanics of the asperities. Our observations, as found in (Shokouhi et al., 2020;  
 451 Wood et al., 2021), show a nearly monotonic relationship between increased permeabil-  
 452 ity enhancement and increased pressure oscillation amplitude. We add to the work of  
 453 (Shokouhi et al., 2020; Manogharan et al., 2021; Wood et al., 2021) by documenting a  
 454 reduction in pore pressure oscillation-induced permeability enhancement with increas-  
 455 ing normal stress on the fracture and related fracture closure. Similar trends are observed  
 456 for the nonlinearity parameters  $\alpha$  and  $\beta$ . For some transmitter-receiver pairs, the non-  
 457 linearity parameters depend on the degree of fracture openness (in the corresponding re-  
 458 gion of the fracture) immediately before oscillation. There is a noticeable increase in non-  
 459 linearity,  $\alpha$  and  $\beta$ , from 10 MPa to 12.5 MPa, for example (see Figures 7b and 8b). That  
 460 is to say, the dominating factor is not necessarily the stress state, but the local fracture  
 461 aperture.

462 We investigate the spatial heterogeneity of nonlinearity parameters with regard to  
 463 actual estimations of fracture contacts and voids. To that end, pressure sensitive film  
 464 images are related to ultrasonic measurements; a smaller initial contact area ( $S_0$ ) is as-  
 465 sociated with higher nonlinearity  $\beta$  and a larger  $S_0$  with a smaller  $\beta$ . To our knowledge,  
 466 this is the first experimental results relating fracture true contact area and elastodynamic  
 467 nonlinearity. Although the evolution of contact asperities ( $\Delta S/S_0$ ) proved to be diffi-  
 468 cult to measure, our results, though scattered, suggest that, smaller changes in contact  
 469 area are correlated with a higher degree of nonlinearity and vice versa, see Figure 16.

470 Finally, we document the rate of recovery from post-oscillation state of permeabil-  
 471 ity and wave velocity. The rate of permeability recovery (log-time) increases above  $\sim$   
 472 0.4 – 0.6 MPa amplitude oscillations at lower stresses ( $\sigma_{\text{eff}} < 17.5\text{MPa}$ ) and oscilla-  
 473 tion amplitude-invariant at higher stresses ( $\sigma_{\text{eff}} > 15\text{MPa}$ ), (see Figure 13). These re-  
 474 covery rates are orders of magnitude smaller than those reported in previous studies (Shokouhi  
 475 et al., 2020; Wood et al., 2021), where gouge present at the fracture interface dominated  
 476 permeability changes. During the unloading phase, the rate of recovery increases with

477 decreasing stress state. These recovery rates are also smaller than in previous studies (Shokouhi  
 478 et al., 2020; Wood et al., 2021), suggesting "accumulated deformation" throughout the  
 479 loading phase of the experiment.

## 480 Data Availability Statement

481 Data for hydraulic, mechanical, and ultrasonic (time delay) for this research are  
 482 available at <https://doi.org/10.5281/zenodo.7392037>.

## 483 Acknowledgments

484 Technical assistance from Steven Swavely is gratefully acknowledged. This work was fully  
 485 supported by a grant from DOE Office of Basic Energy Science (DE-SC0017585) to PS.  
 486 CM acknowledges support from the European Research Council Advance Grant 835012  
 487 (TECTONIC) and US Department of Energy grants DE-SC0020512 and DE-EE0008763.

## 488 References

- 489 Boettcher, M., & Marone, C. (2004). Effects of normal stress variation on the  
 490 strength and stability of creeping faults. *Journal of Geophysical Research: Solid Earth*, *109*(B3).  
 491
- 492 Brenguier, F., Campillo, M., Hadziioannou, C., Shapiro, N. M., Nadeau, R. M.,  
 493 & Larose, E. (2008). Postseismic relaxation along the san andreas fault at  
 494 parkfield from continuous seismological observations. *Science*, *321*(5895),  
 495 1478–1481. Retrieved from [https://science.sciencemag.org/content/321/](https://science.sciencemag.org/content/321/5895/1478)  
 496 [5895/1478](https://science.sciencemag.org/content/321/5895/1478) doi: 10.1126/science.1160943
- 497 Brodsky, E. E., & Lajoie, L. J. (2013). Anthropogenic seismicity rates and opera-  
 498 tional parameters at the salton sea geothermal field. *Science*, *341*(6145), 543-  
 499 546. Retrieved from [https://www.science.org/doi/abs/10.1126/science](https://www.science.org/doi/abs/10.1126/science.1239213)  
 500 [.1239213](https://www.science.org/doi/abs/10.1126/science.1239213) doi: 10.1126/science.1239213
- 501 Candela, T., Brodsky, E. E., Marone, C., & Elsworth, D. (2014). Laboratory evi-  
 502 dence for particle mobilization as a mechanism for permeability enhancement  
 503 via dynamic stressing. *Earth and Planetary Science Letters*, *392*, 279-291. doi:  
 504 <https://doi.org/10.1016/j.epsl.2014.02.025>
- 505 Candela, T., Brodsky, E. E., Marone, C., & Elsworth, D. (2015). Flow rate dic-  
 506 tates permeability enhancement during fluid pressure oscillations in laboratory  
 507 experiments. *Journal of Geophysical Research: Solid Earth*, *120*(4), 2037-  
 508 2055. Retrieved from [https://agupubs.onlinelibrary.wiley.com/doi/abs/](https://agupubs.onlinelibrary.wiley.com/doi/abs/10.1002/2014JB011511)  
 509 [10.1002/2014JB011511](https://agupubs.onlinelibrary.wiley.com/doi/abs/10.1002/2014JB011511) doi: <https://doi.org/10.1002/2014JB011511>
- 510 Elkhoury, J. E., Niemeijer, A., Brodsky, E. E., & Marone, C. (2011). Laboratory  
 511 observations of permeability enhancement by fluid pressure oscillation of in  
 512 situ fractured rock. *Journal of Geophysical Research: Solid Earth*, *116*(B2).  
 513 Retrieved from [https://agupubs.onlinelibrary.wiley.com/doi/abs/](https://agupubs.onlinelibrary.wiley.com/doi/abs/10.1029/2010JB007759)  
 514 [10.1029/2010JB007759](https://agupubs.onlinelibrary.wiley.com/doi/abs/10.1029/2010JB007759) doi: <https://doi.org/10.1029/2010JB007759>
- 515 Guyer, R. A., & Johnson, P. A. (2009). *Nonlinear mesoscopic elasticity: the complex*  
 516 *behaviour of rocks, soil, concrete*. John Wiley & Sons.
- 517 Healy, J. H., Rubey, W. W., Griggs, D. T., & Raleigh, C. B. (1968). The  
 518 denver earthquakes. *Science*, *161*(3848), 1301–1310. Retrieved from  
 519 <https://science.sciencemag.org/content/161/3848/1301> doi:  
 520 [10.1126/science.161.3848.1301](https://science.sciencemag.org/content/161/3848/1301)
- 521 Hedayat, A., Pyrak-Nolte, L. J., & Bobet, A. (2014, August). Precursors to the  
 522 shear failure of rock discontinuities: Precursors to Rock Frictional Sliding.  
 523 *Geophys. Res. Lett.*, *41*(15), 5467–5475. Retrieved 2022-02-07, from [http://](http://doi.wiley.com/10.1002/2014GL060848)  
 524 [doi.wiley.com/10.1002/2014GL060848](http://doi.wiley.com/10.1002/2014GL060848) doi: 10.1002/2014GL060848

- 525 Hertz, H. (1881). On the contact of elastic solids. *Z. Reine Angew. Mathematik*, *92*,  
526 156–171.
- 527 Ishibashi, T., Elsworth, D., Fang, Y., Rivière, J., Madara, B., Asanuma, H., ...  
528 Marone, C. (2018). Friction-stability-permeability evolution of a fracture  
529 in granite. *Water Resources Research*, *54*(12), 9901–9918. Retrieved  
530 from [https://agupubs.onlinelibrary.wiley.com/doi/abs/10.1029/](https://agupubs.onlinelibrary.wiley.com/doi/abs/10.1029/2018WR022598)  
531 [2018WR022598](https://doi.org/10.1029/2018WR022598) doi: <https://doi.org/10.1029/2018WR022598>
- 532 Jin, J., Johnson, P., & Shokouhi, P. (2020). An integrated analytical and experimen-  
533 tal study of contact acoustic nonlinearity at rough interfaces of fatigue cracks.  
534 *Journal of the Mechanics and Physics of Solids*, *135*, 103769.
- 535 Johnson, P., & Sutin, A. (2005). Slow dynamics and anomalous nonlinear fast dy-  
536 namics in diverse solids. *The Journal of the Acoustical Society of America*,  
537 *117*(1), 124–130. Retrieved from <https://doi.org/10.1121/1.1823351> doi:  
538 [10.1121/1.1823351](https://doi.org/10.1121/1.1823351)
- 539 Johnson, P. A., Carmeliet, J., Savage, H. M., Scuderi, M., Carpenter, B. M.,  
540 Guyer, R. A., ... Marone, C. (2016). Dynamically triggered slip lead-  
541 ing to sustained fault gouge weakening under laboratory shear conditions.  
542 *Geophysical Research Letters*, *43*(4), 1559–1565. Retrieved from [https://](https://agupubs.onlinelibrary.wiley.com/doi/abs/10.1002/2015GL067056)  
543 [agupubs.onlinelibrary.wiley.com/doi/abs/10.1002/2015GL067056](https://doi.org/10.1002/2015GL067056) doi:  
544 <https://doi.org/10.1002/2015GL067056>
- 545 Liu, W., & Manga, M. (2009). Changes in permeability caused by dynamic stresses  
546 in fractured sandstone. *Geophysical Research Letters*, *36*(20).
- 547 Manogharan, P., Wood, C., Marone, C., Elsworth, D., Rivière, J., & Shokouhi,  
548 P. (2021). Nonlinear elastodynamic behavior of intact and fractured  
549 rock under in-situ stress and saturation conditions. *Journal of the Me-*  
550 *chanics and Physics of Solids*, *153*, 104491. Retrieved from [https://](https://www.sciencedirect.com/science/article/pii/S0022509621001605)  
551 [www.sciencedirect.com/science/article/pii/S0022509621001605](https://doi.org/10.1016/j.jmps.2021.104491) doi:  
552 <https://doi.org/10.1016/j.jmps.2021.104491>
- 553 McGarr, A., Bekins, B., Burkardt, N., Dewey, J., Earle, P., Ellsworth, W., ... Shee-  
554 han, A. (2015). Coping with earthquakes induced by fluid injection. *Science*,  
555 *347*(6224), 830–831. Retrieved from [https://science.sciencemag.org/](https://science.sciencemag.org/content/347/6224/830)  
556 [content/347/6224/830](https://doi.org/10.1126/science.aaa0494) doi: [10.1126/science.aaa0494](https://doi.org/10.1126/science.aaa0494)
- 557 McNamara, D. E., Hayes, G. P., Benz, H. M., Williams, R. A., McMahon, N. D.,  
558 Aster, R. C., ... Earle, P. (2015). Reactivated faulting near cushioning, ok-  
559 lahoma: Increased potential for a triggered earthquake in an area of united  
560 states strategic infrastructure. *Geophysical Research Letters*, *42*(20), 8328-  
561 8332. Retrieved from [https://agupubs.onlinelibrary.wiley.com/doi/abs/](https://agupubs.onlinelibrary.wiley.com/doi/abs/10.1002/2015GL064669)  
562 [10.1002/2015GL064669](https://doi.org/10.1002/2015GL064669) doi: <https://doi.org/10.1002/2015GL064669>
- 563 Raleigh, C. B., Healy, J. H., & Bredehoeft, J. D. (1976). An experiment in earth-  
564 quake control at Rangely, Colorado. *Science*, *191*(4233), 1230–1237. Retrieved  
565 from <https://science.sciencemag.org/content/191/4233/1230> doi: [10](https://doi.org/10.1126/science.191.4233.1230)  
566 [.1126/science.191.4233.1230](https://doi.org/10.1126/science.191.4233.1230)
- 567 Rivière, J., Renaud, G., Guyer, R. A., & Johnson, P. A. (2013). Pump and probe  
568 waves in dynamic acousto-elasticity: Comprehensive description and com-  
569 parison with nonlinear elastic theories. *Journal of Applied Physics*, *114*(5),  
570 054905. Retrieved from <https://doi.org/10.1063/1.4816395> doi:  
571 [10.1063/1.4816395](https://doi.org/10.1063/1.4816395)
- 572 Rivière, J., Shokouhi, P., Guyer, R. A., & Johnson, P. A. (2015). A set of measures  
573 for the systematic classification of the nonlinear elastic behavior of disparate  
574 rocks. *Journal of Geophysical Research: Solid Earth*, *120*(3), 1587–1604.  
575 Retrieved from [https://agupubs.onlinelibrary.wiley.com/doi/abs/](https://agupubs.onlinelibrary.wiley.com/doi/abs/10.1002/2014JB011718)  
576 [10.1002/2014JB011718](https://doi.org/10.1002/2014JB011718) doi: <https://doi.org/10.1002/2014JB011718>
- 577 Rivière, J., Pimienta, L., Scuderi, M., Candela, T., Shokouhi, P., Fortin, J., ...  
578 Johnson, P. A. (2016). Frequency, pressure, and strain dependence of nonlin-  
579 ear elasticity in Berea sandstone. *Geophysical Research Letters*, *43*(7), 3226-

- 580 3236. Retrieved from [https://agupubs.onlinelibrary.wiley.com/doi/abs/](https://agupubs.onlinelibrary.wiley.com/doi/abs/10.1002/2016GL068061)  
581 10.1002/2016GL068061 doi: <https://doi.org/10.1002/2016GL068061>
- 582 Roberts, P. M. (2005). Laboratory observations of altered porous fluid flow behavior  
583 in Berea sandstone induced by low-frequency dynamic stress stimulation.  
584 *Acoustical Physics*, 51, S140-S148.
- 585 Roberts, P. M., & Abdel-Fattah, A. I. (2009). Seismic stress stimulation mobilizes  
586 colloids trapped in a porous rock. *Earth and Planetary Science Letters*, 284(3-  
587 4), 538–543.
- 588 Roux, P., Marandet, C., Nicolas, B., & Kuperman, W. A. (2013, July). Experimental  
589 measurement of the acoustic sensitivity kernel. *The Journal of*  
590 *the Acoustical Society of America*, 134(1), EL38–EL44. Retrieved 2022-  
591 02-09, from <http://asa.scitation.org/doi/10.1121/1.4808111> doi:  
592 10.1121/1.4808111
- 593 Savage, H. M., & Marone, C. (2007). Effects of shear velocity oscillations on stick-  
594 slip behavior in laboratory experiments. *Journal of Geophysical Research:*  
595 *Solid Earth*, 112(B2).
- 596 Shokouhi, P., Jin, J., Wood, C., Rivière, J., Madara, B., Elsworth, D., & Marone,  
597 C. (2020). Dynamic stressing of naturally fractured rocks: On the relation  
598 between transient changes in permeability and elastic wave velocity. *Geo-*  
599 *physical Research Letters*, 47(1), e2019GL083557. Retrieved from [https://](https://agupubs.onlinelibrary.wiley.com/doi/abs/10.1029/2019GL083557)  
600 [agupubs.onlinelibrary.wiley.com/doi/abs/10.1029/2019GL083557](https://agupubs.onlinelibrary.wiley.com/doi/abs/10.1029/2019GL083557)  
601 (e2019GL083557 2019GL083557) doi: <https://doi.org/10.1029/2019GL083557>
- 602 Shokouhi, P., Rivière, J., Guyer, R. A., & Johnson, P. A. (2017). Slow dynamics of  
603 consolidated granular systems: Multi-scale relaxation. *Applied Physics Letters*,  
604 111(25), 251604. Retrieved from <https://doi.org/10.1063/1.5010043> doi:  
605 10.1063/1.5010043
- 606 Shreedharan, S., Bolton, D. C., Rivière, J., & Marone, C. (2021, January). Com-  
607 petition between preslip and deviatoric stress modulates precursors for lab-  
608 oratory earthquakes. *Earth and Planetary Science Letters*, 553, 116623.  
609 Retrieved 2022-02-07, from [https://linkinghub.elsevier.com/retrieve/](https://linkinghub.elsevier.com/retrieve/pii/S0012821X20305677)  
610 [pii/S0012821X20305677](https://linkinghub.elsevier.com/retrieve/pii/S0012821X20305677) doi: 10.1016/j.epsl.2020.116623
- 611 Simpson, D., Leith, W., & Scholz, C. (1988, 12). Two types of reservoir-induced seis-  
612 micity. *Bulletin of the Seismological Society of America*, 78(6), 2025-2040.
- 613 Sminchak, J., & Gupta, N. (2003, 06). Aspects of induced seismic activity and deep-  
614 well sequestration of carbon dioxide. *Environmental Geosciences*, 10(2), 81-89.  
615 Retrieved from <https://doi.org/10.1306/eg.04040302009> doi: 10.1306/eg  
616 .04040302009
- 617 Spetzler, J., & Snieder, R. (2004, May). The Fresnel volume and transmitted waves.  
618 *GEOPHYSICS*, 69(3), 653–663. Retrieved 2022-02-09, from [https://library](https://library.seg.org/doi/10.1190/1.1759451)  
619 [.seg.org/doi/10.1190/1.1759451](https://library.seg.org/doi/10.1190/1.1759451) doi: 10.1190/1.1759451
- 620 van der Elst, N. J., Savage, H. M., Keranen, K. M., & Abers, G. A. (2013). En-  
621 hanced remote earthquake triggering at fluid-injection sites in the mid-  
622 western United States. *Science*, 341(6142), 164-167. Retrieved from  
623 <https://www.science.org/doi/abs/10.1126/science.1238948> doi:  
624 10.1126/science.1238948
- 625 Walsh, F. R., & Zoback, M. D. (2015). Oklahoma's recent earthquakes and salt-  
626 water disposal. *Science Advances*, 1(5). Retrieved from [https://advances](https://advances.sciencemag.org/content/1/5/e1500195)  
627 [.sciencemag.org/content/1/5/e1500195](https://advances.sciencemag.org/content/1/5/e1500195) doi: 10.1126/sciadv.1500195
- 628 Wood, C., Shokouhi, P., Manogharan, P., Rivère, J., Elsworth, D., & Marone, C.  
629 (2021). Imaging elastodynamic and hydraulic properties of in situ fractured  
630 rock: An experimental investigation exploring effects of dynamic stress-  
631 ing and shearing. *Journal of Geophysical Research: Solid Earth*, 126(11),  
632 e2020JB021521. Retrieved from [https://agupubs.onlinelibrary.wiley](https://agupubs.onlinelibrary.wiley.com/doi/abs/10.1029/2020JB021521)  
633 [.com/doi/abs/10.1029/2020JB021521](https://agupubs.onlinelibrary.wiley.com/doi/abs/10.1029/2020JB021521) (e2020JB021521 2020JB021521) doi:  
634 <https://doi.org/10.1029/2020JB021521>

- 635 Zhang, F., Fang, Y., Elsworth, D., Wang, C., & Yang, X. (2017). Evolution of Fric-  
636 tion and Permeability in a Propped Fracture under Shear. *Geofluids*, 2017,  
637 2063747. Retrieved from <https://doi.org/10.1155/2017/2063747> doi:  
638 10.1155/2017/2063747
- 639 Zhang, Y., Nishizawa, O., Kiyama, T., & Xue, Z. (2015, July). Saturation-path de-  
640 pendency of P-wave velocity and attenuation in sandstone saturated with CO  
641 2 and brine revealed by simultaneous measurements of waveforms and X-ray  
642 computed tomography images. *GEOPHYSICS*, 80(4), D403–D415. Retrieved  
643 2022-02-09, from <https://library.seg.org/doi/10.1190/geo2014-0289.1>  
644 doi: 10.1190/geo2014-0289.1

Figure1.

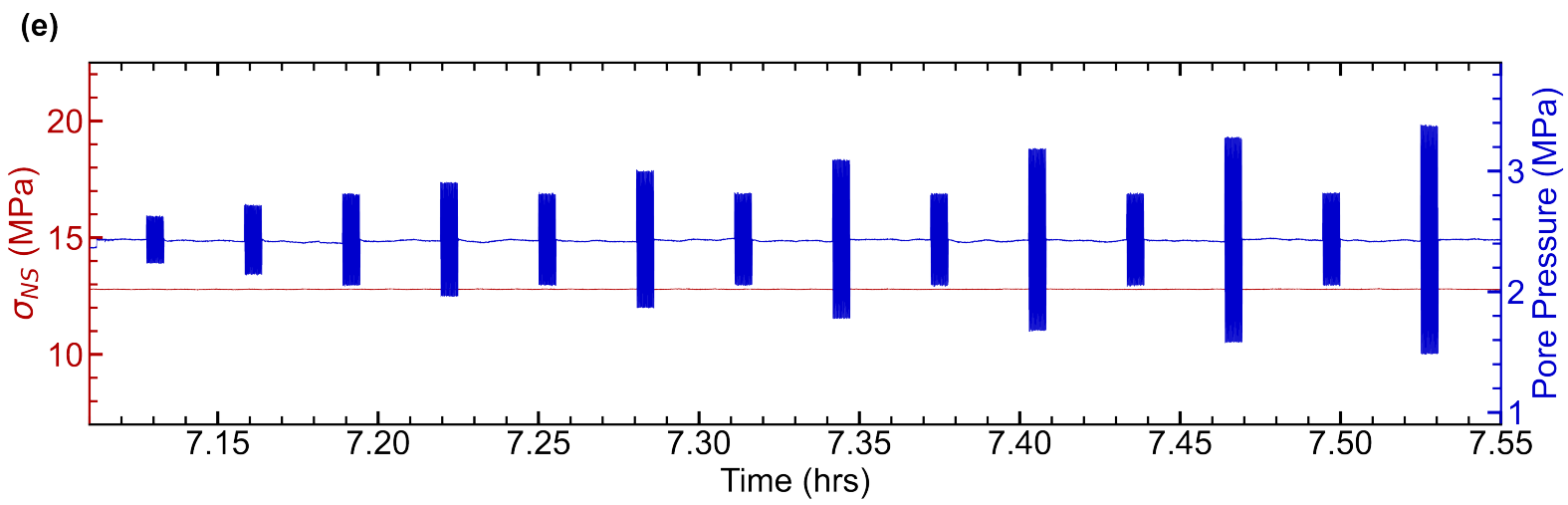
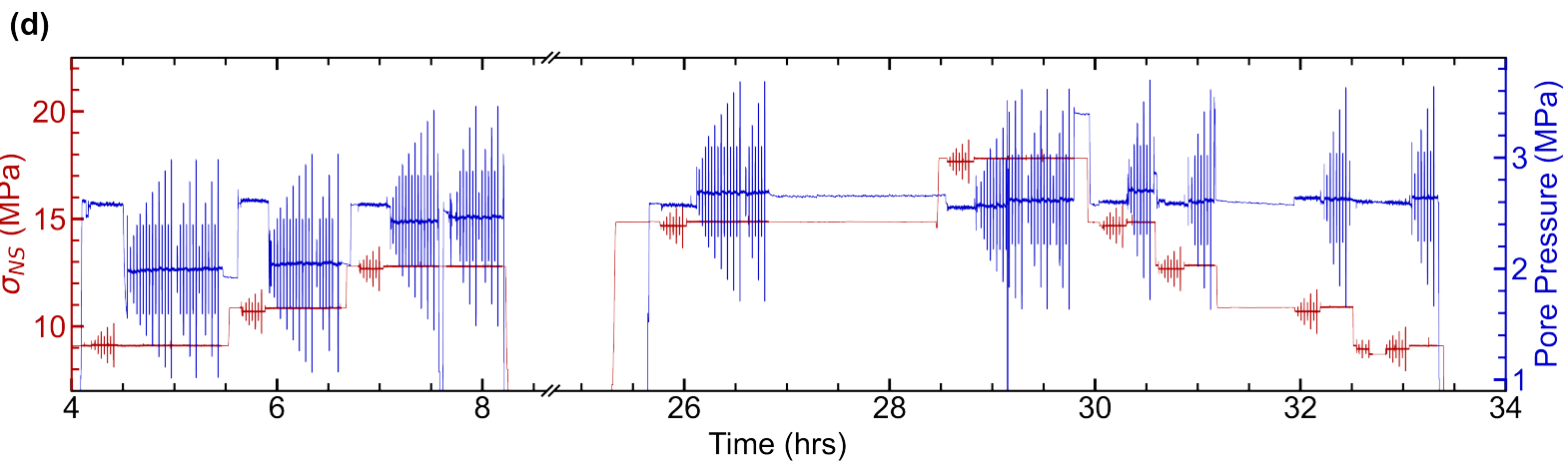
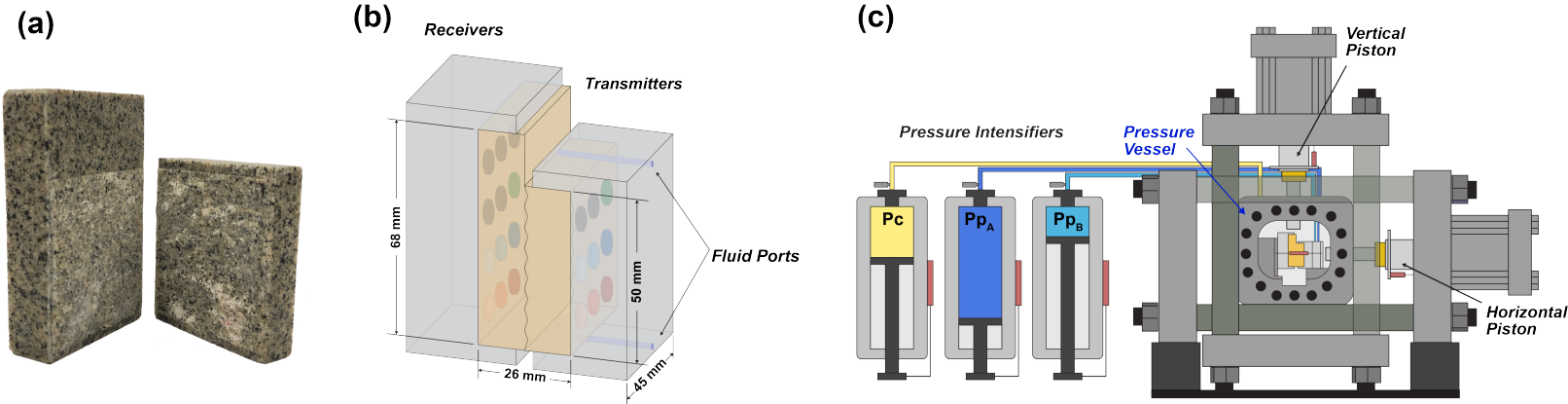


Figure2.

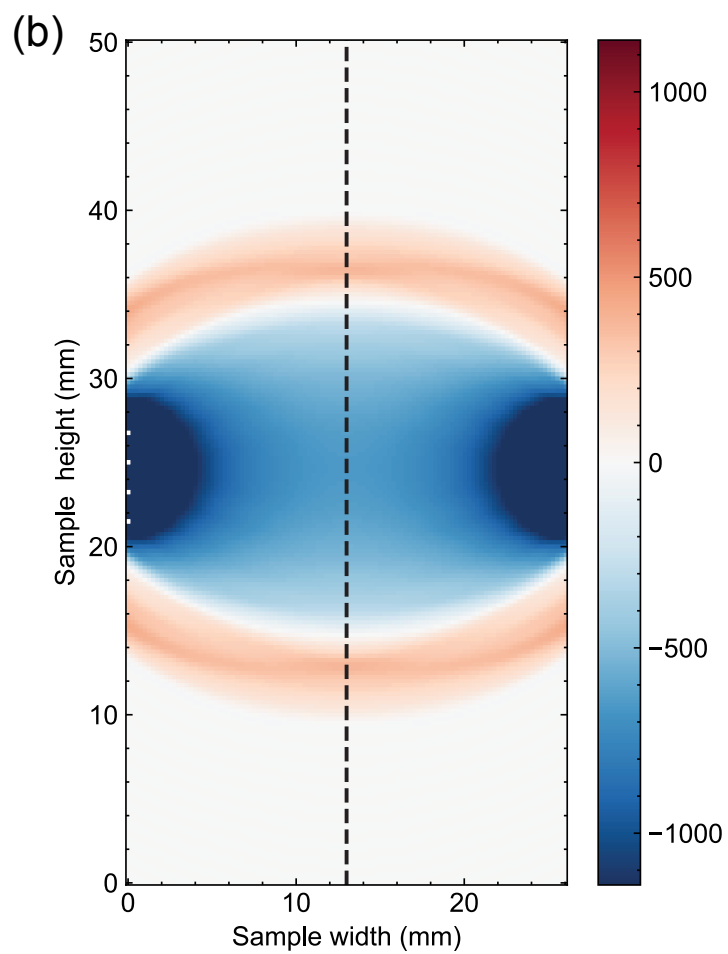
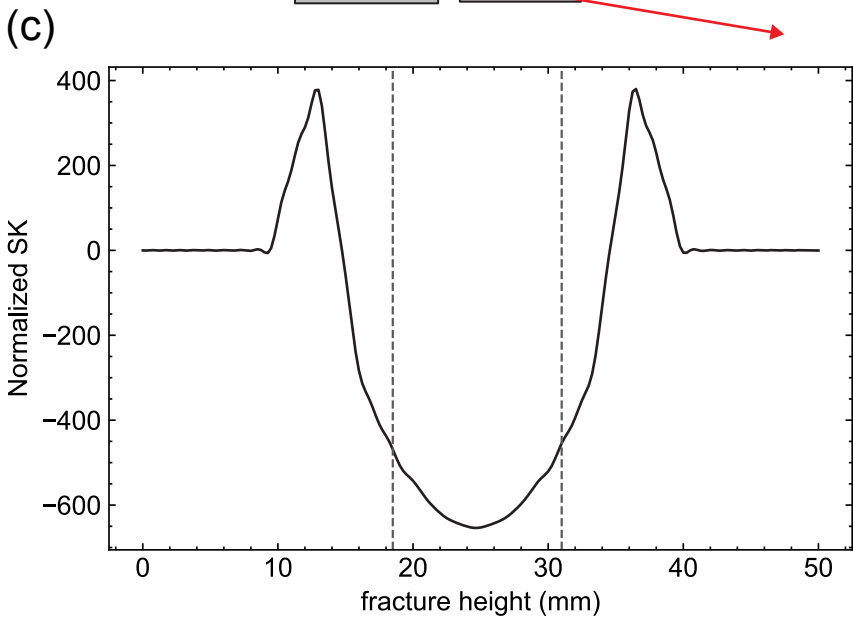
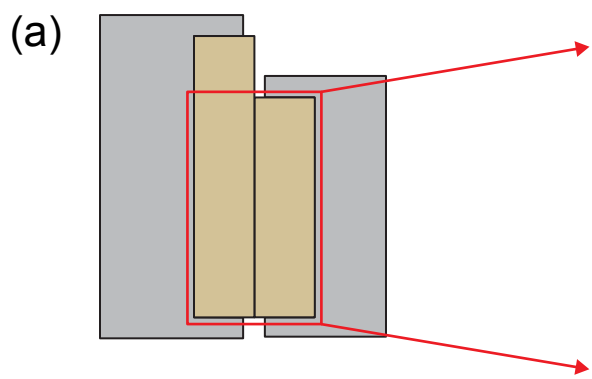


Figure3.

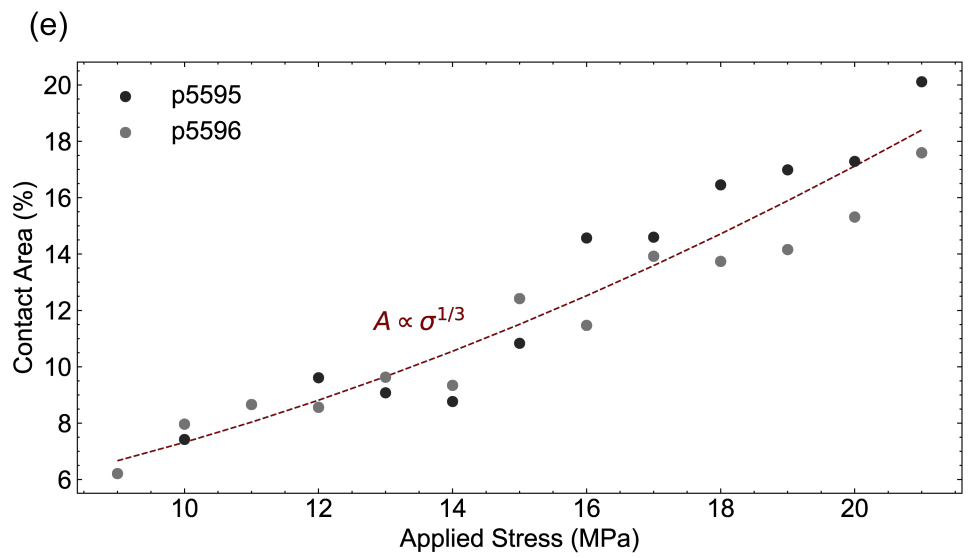
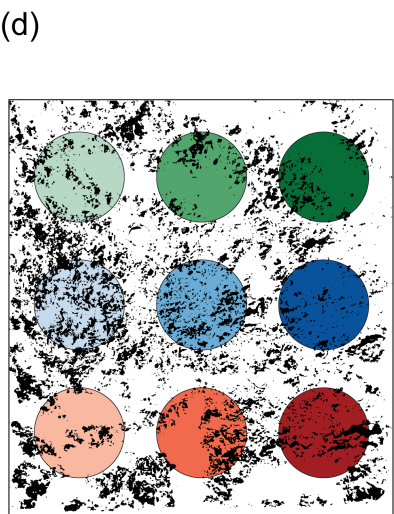
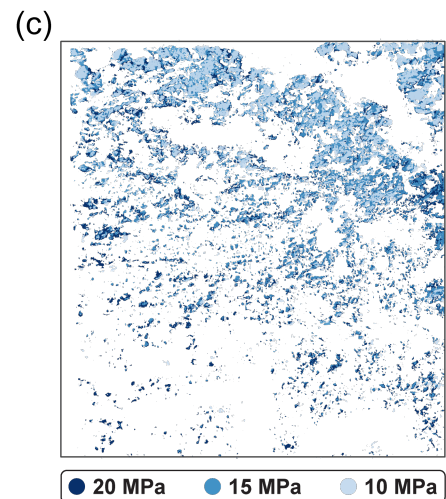
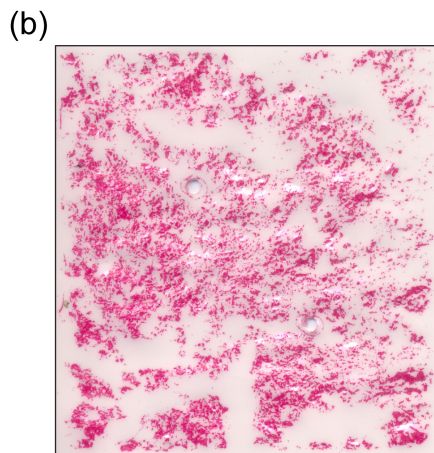
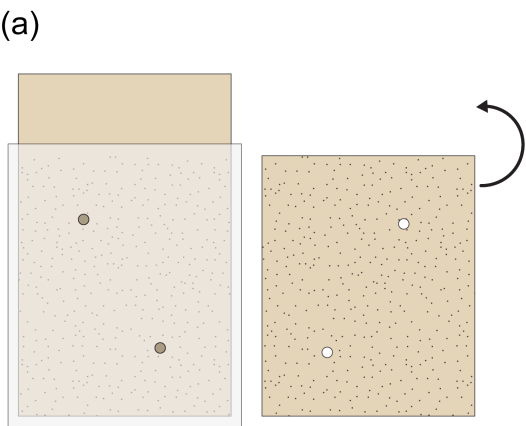


Figure4.

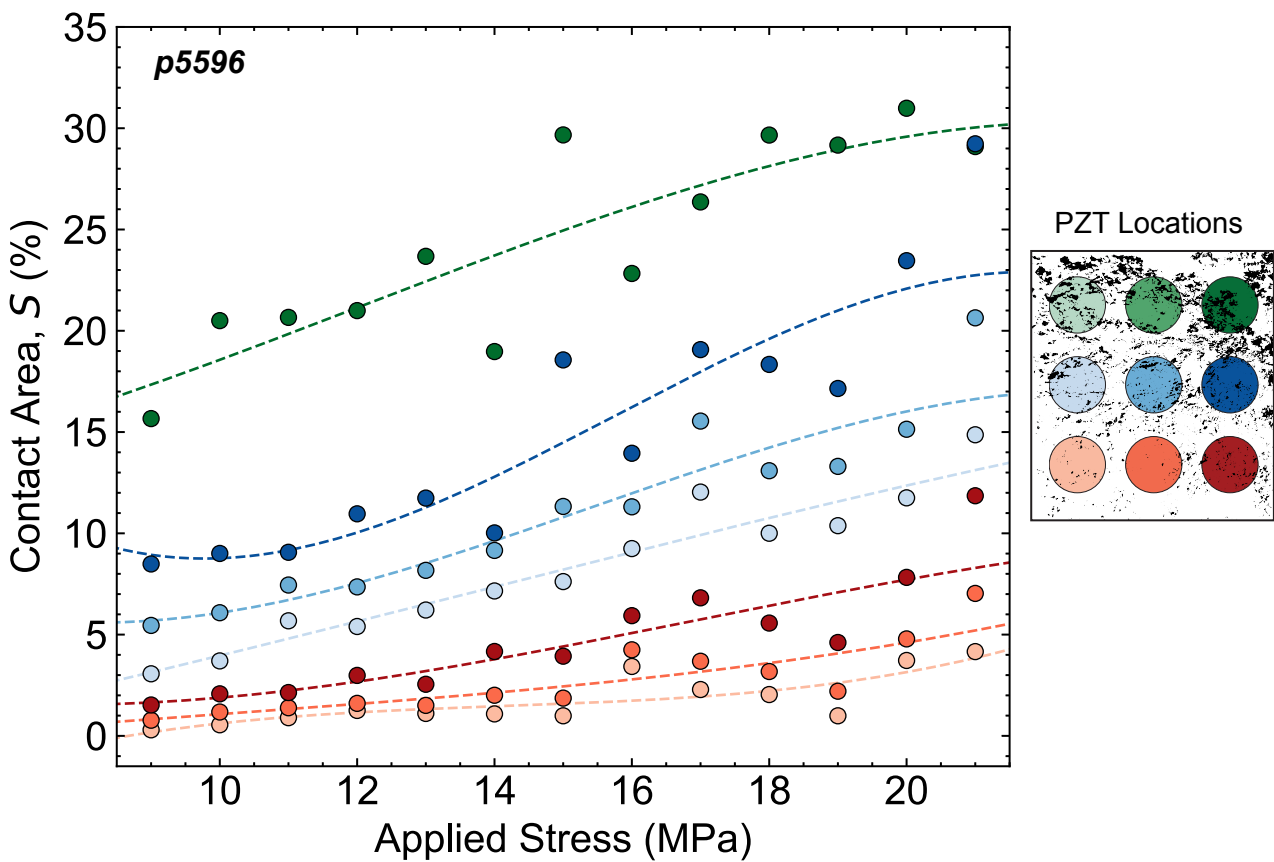


Figure5.

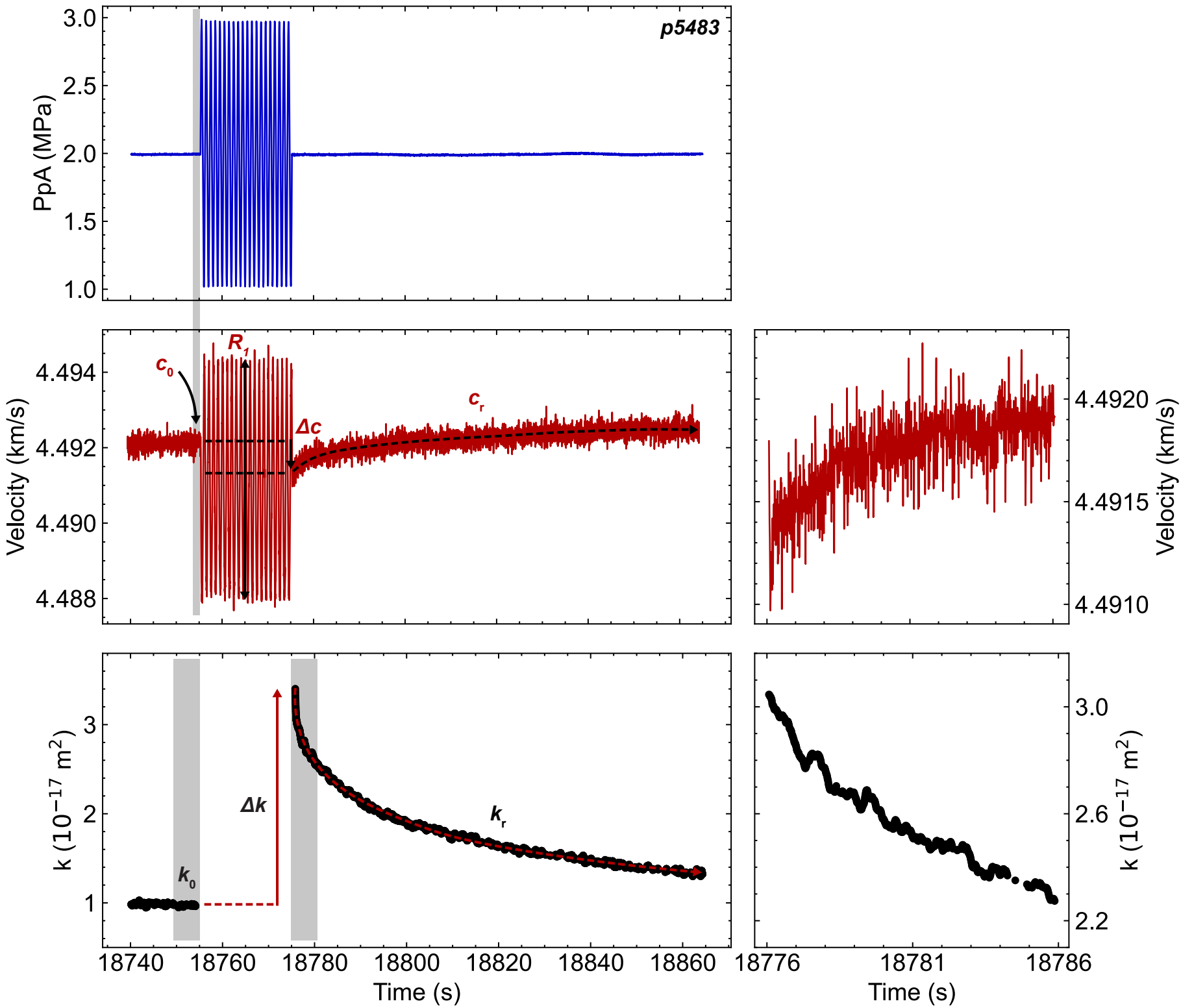


Figure6.

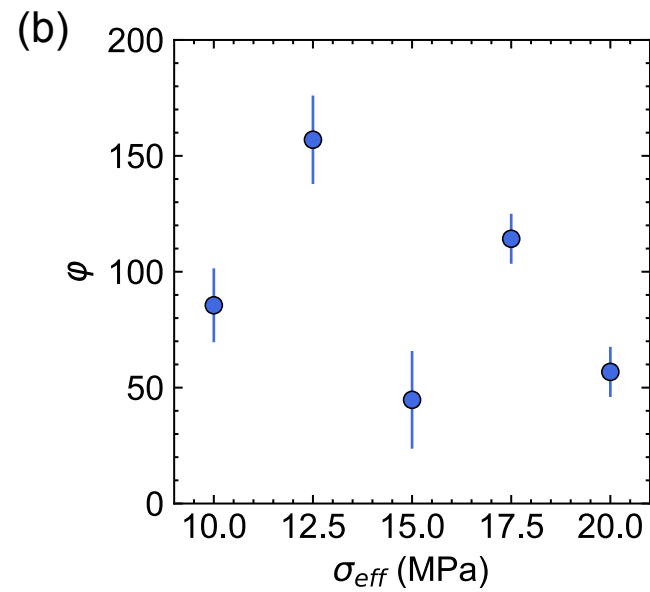
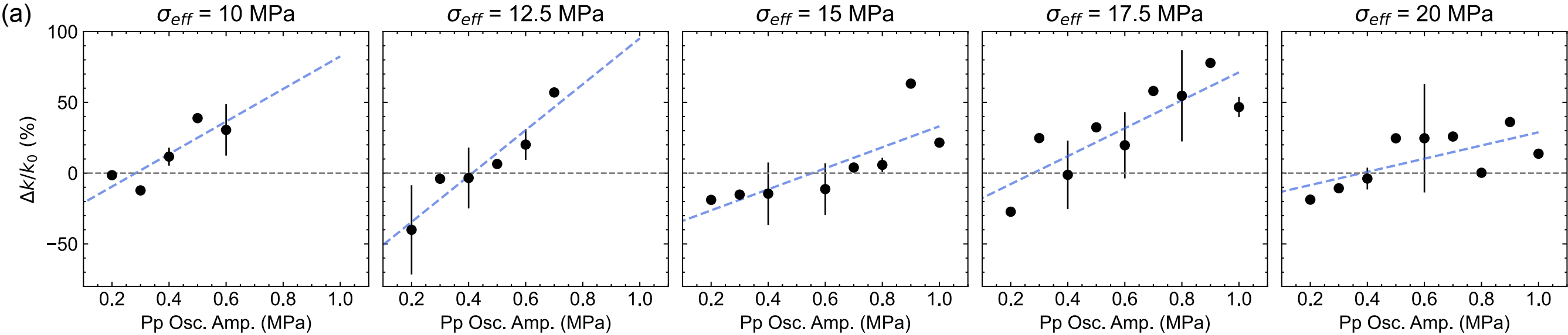


Figure7.

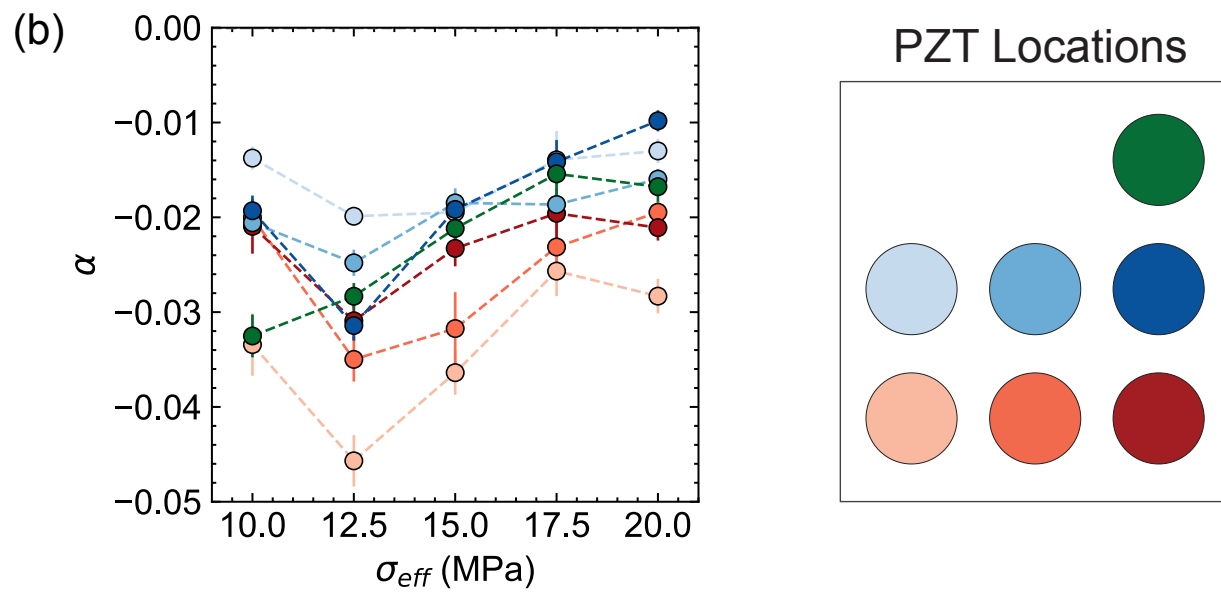
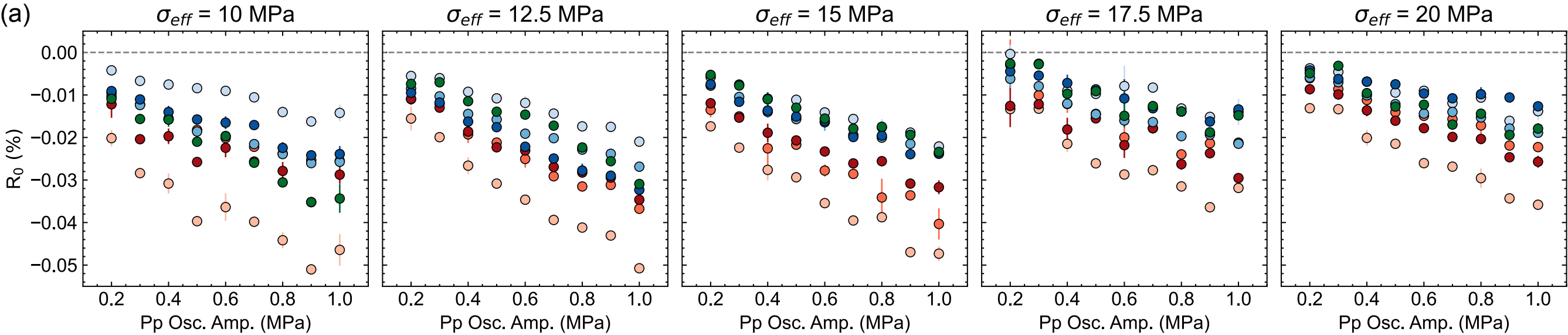


Figure8.

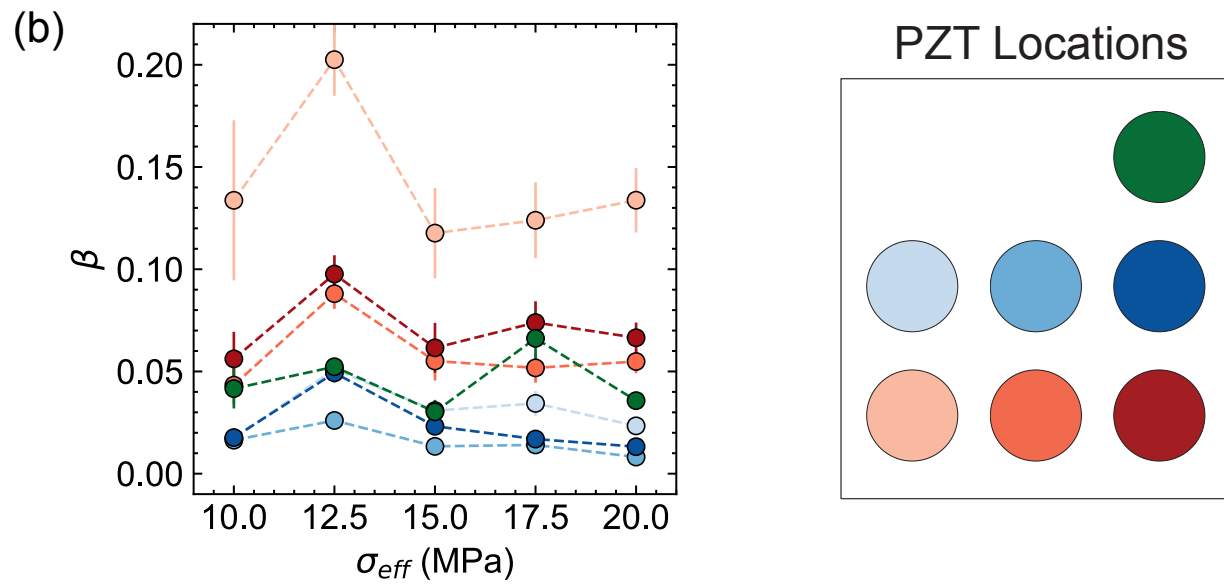
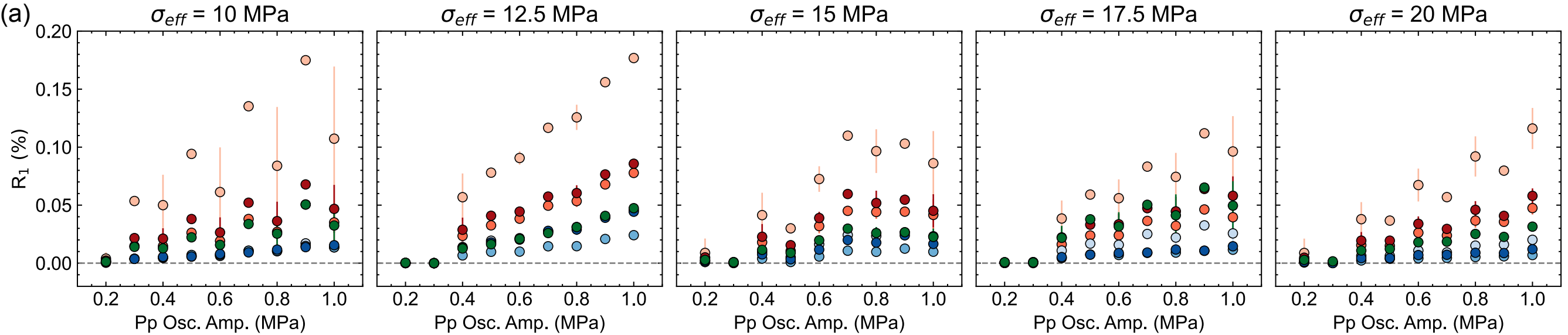


Figure9.

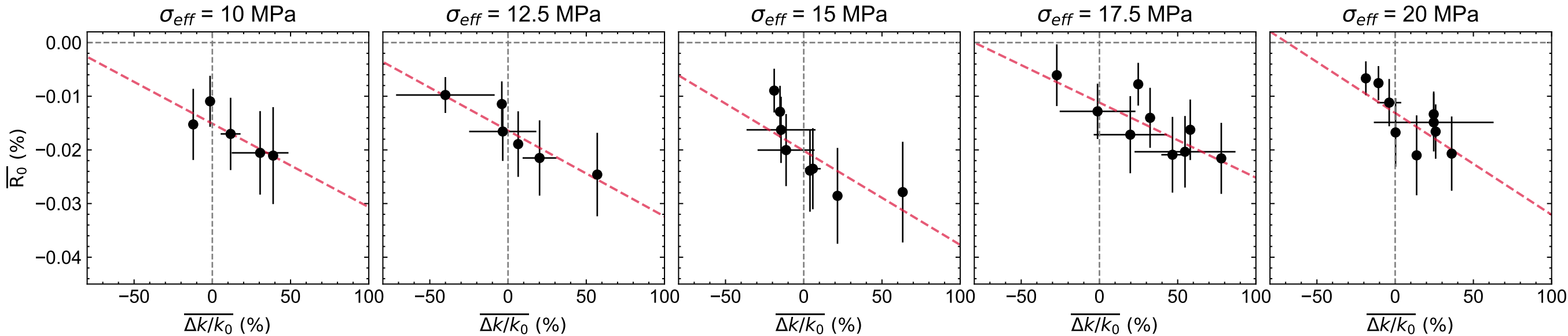


Figure10.

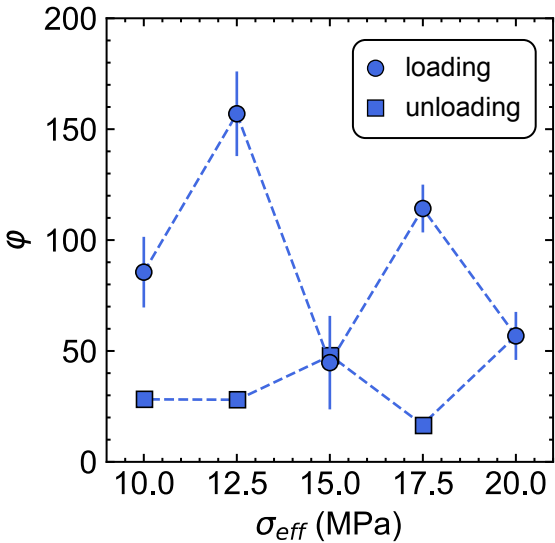


Figure11.

PZT Locations

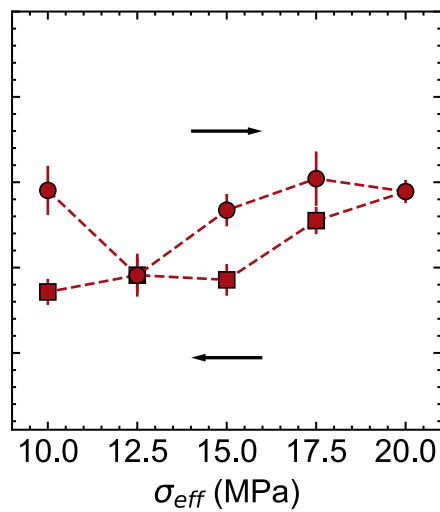
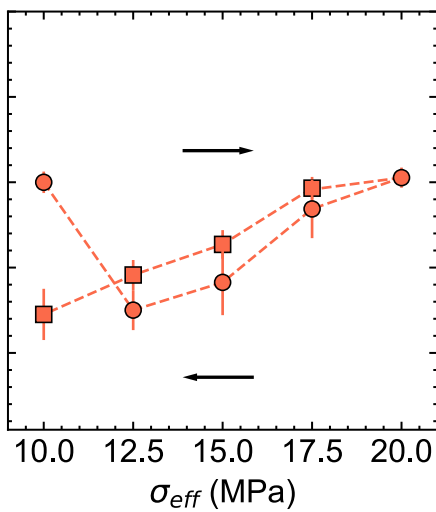
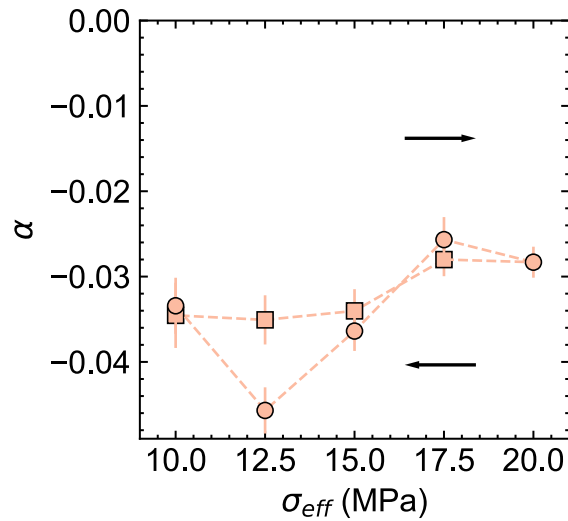
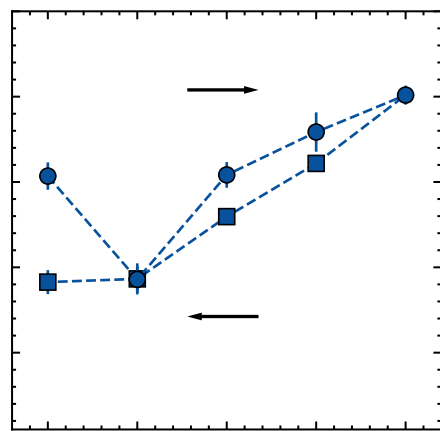
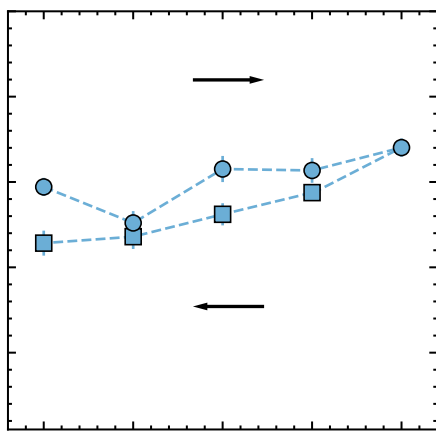
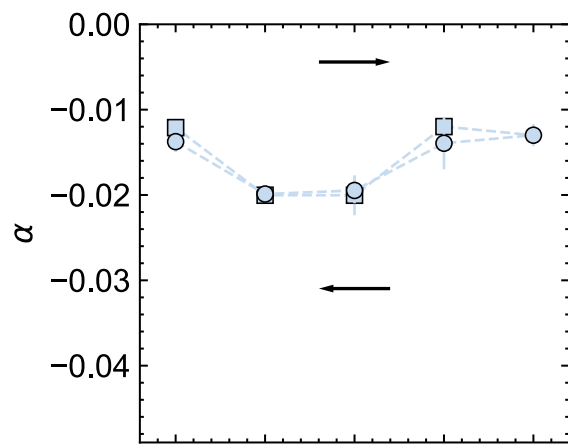
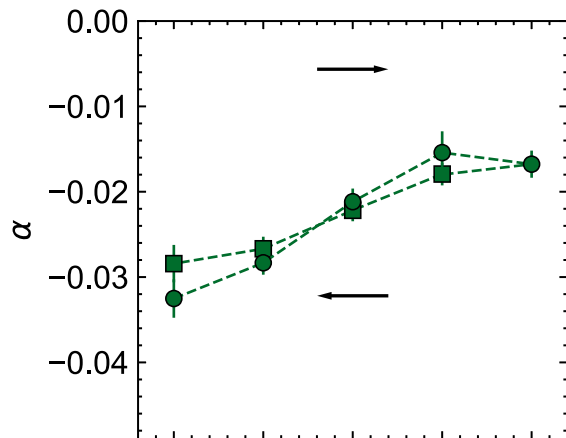
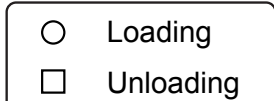
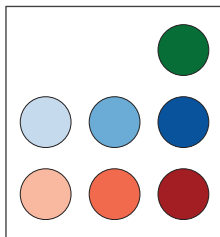


Figure12.

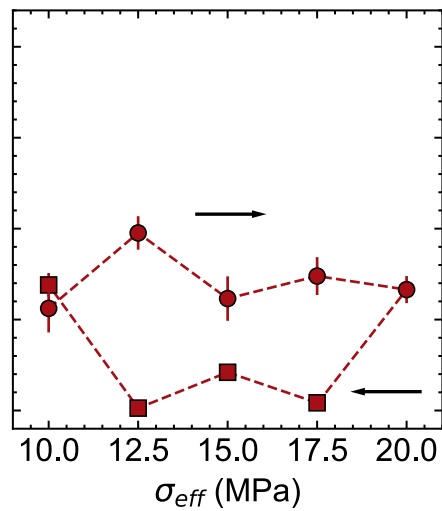
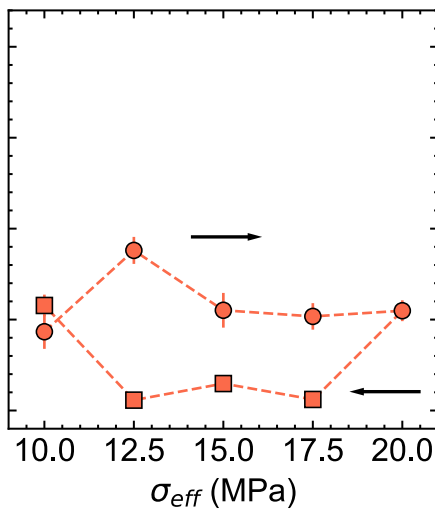
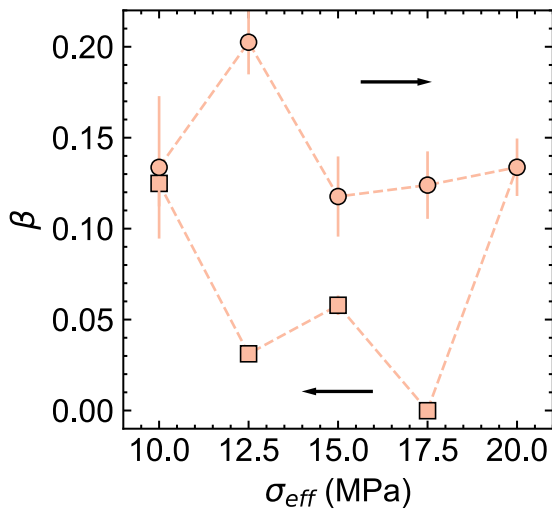
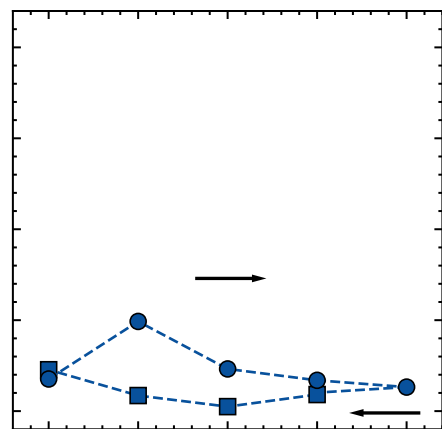
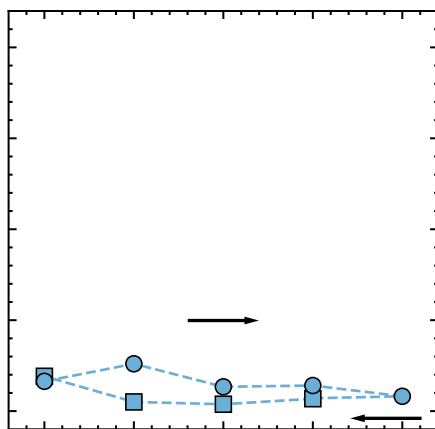
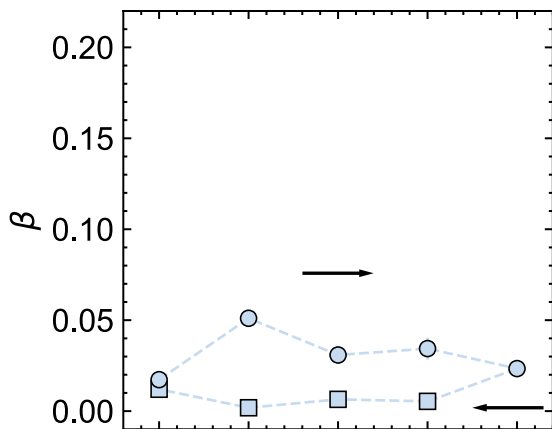
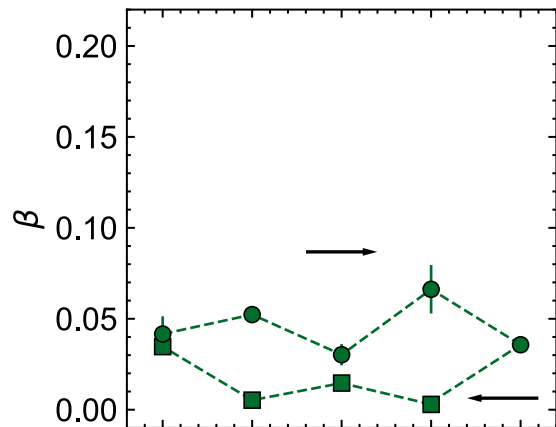
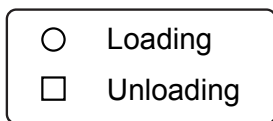
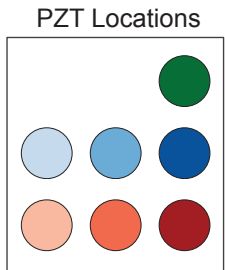


Figure13.

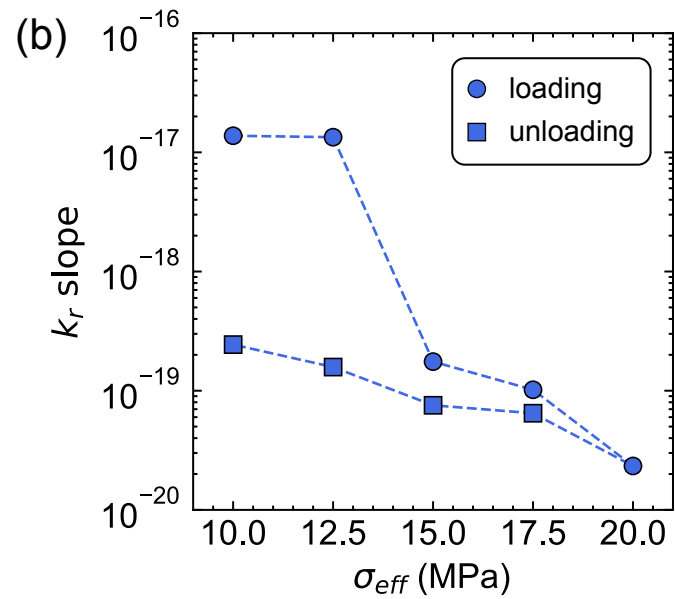
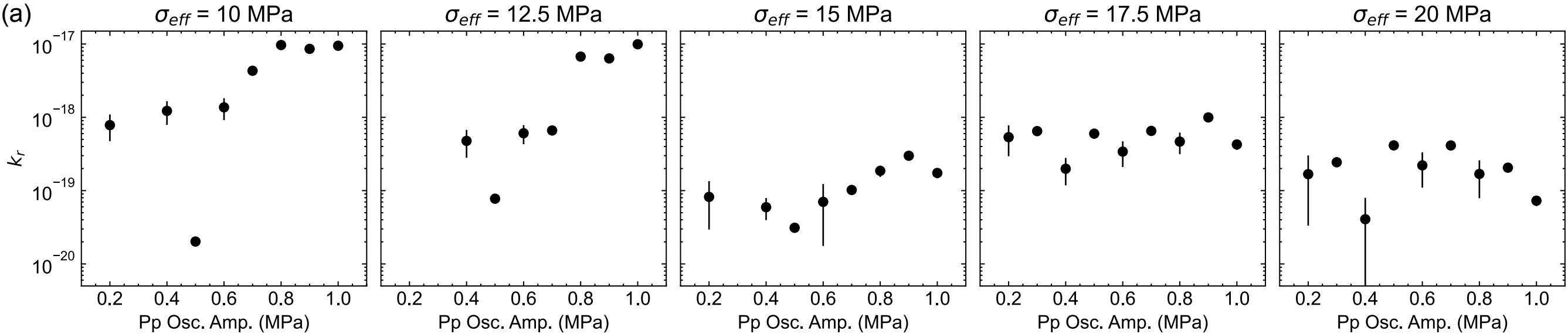


Figure14.

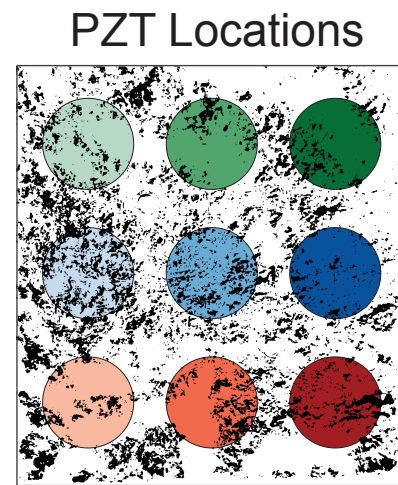
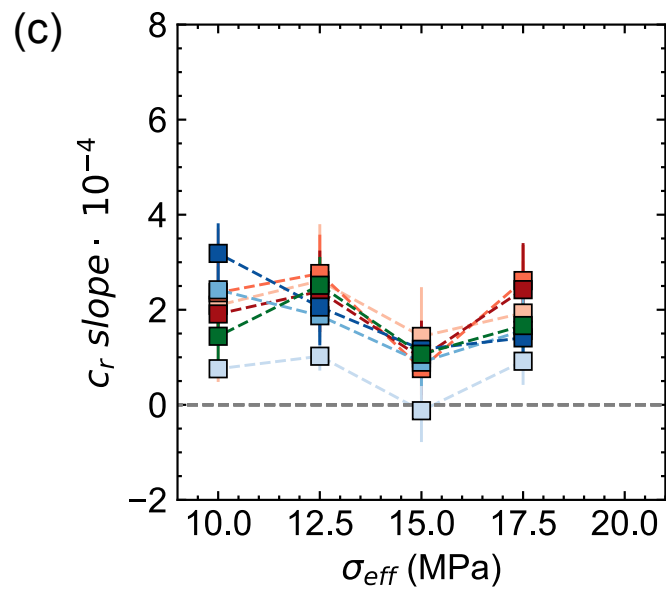
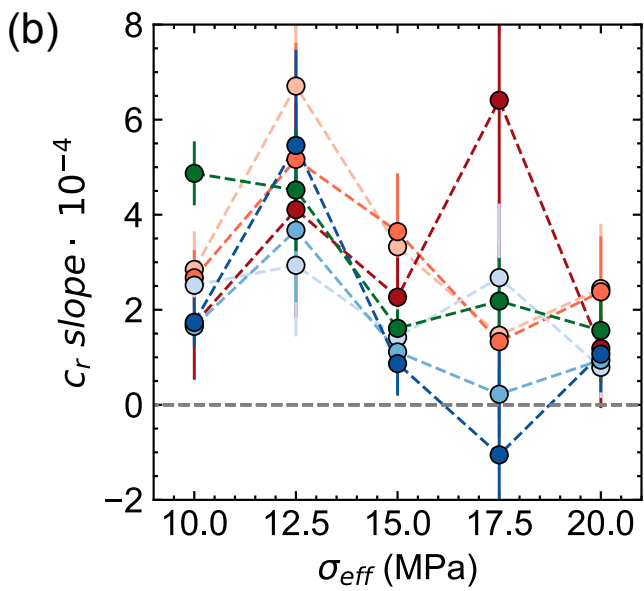
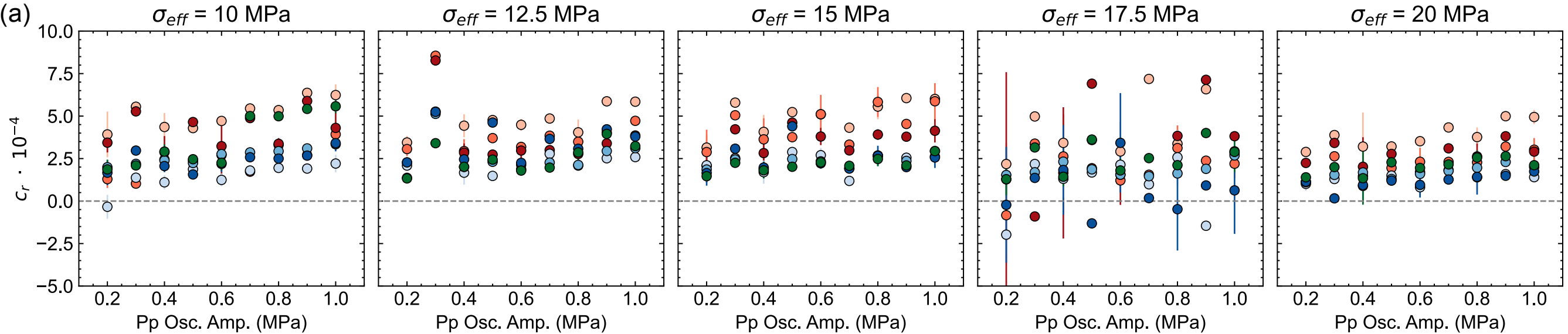


Figure15.

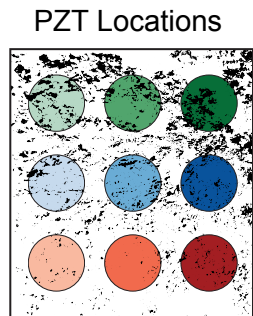
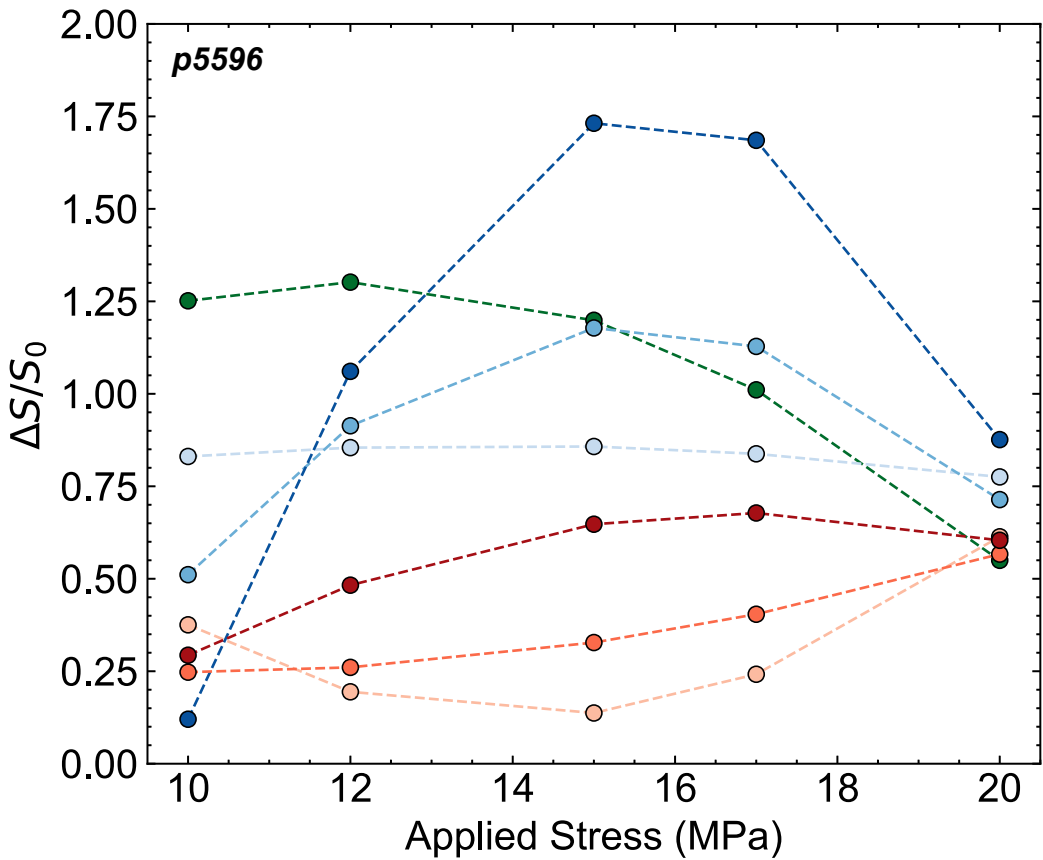


Figure16.

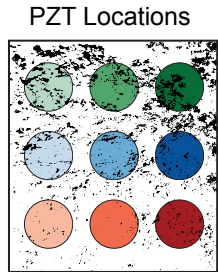
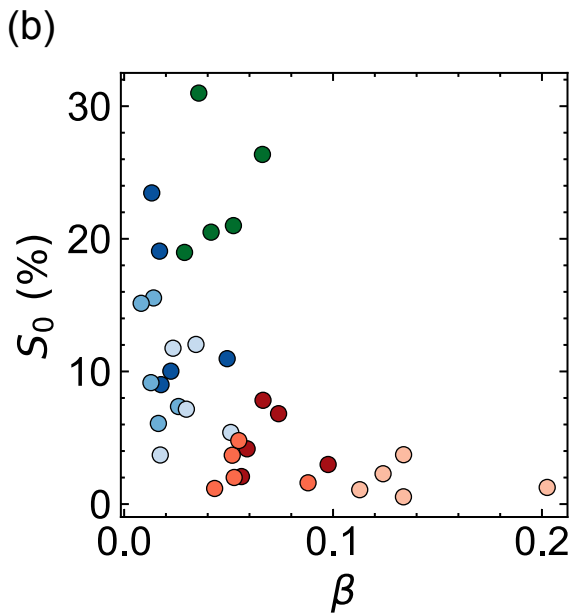
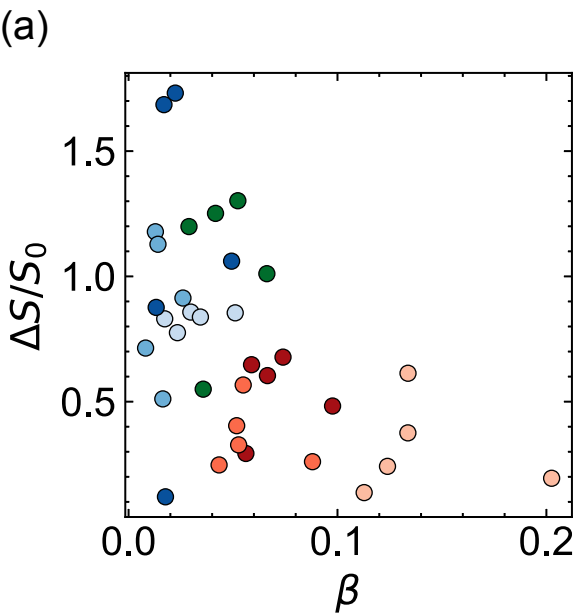


Figure17.

